An Empirical Approach to Modeling Ion Production Rates in Titan's Ionosphere II: Ion Production Rates on the Nightside

M. S. Richard[1,2], T. E. Cravens[1], C. Wylie[1], D Webb[1], Q. Chediak[1], K.Mandt[3], J. H. Waite Jr.[3], A. Rymer[4], C. Bertucci[5], A. Wellbrock[6,7], A. Windsor[2], A. J. Coates[6,7]

1) Department of Physics and Astronomy, University of Kansas, Lawrence, Kansas, USA

2) Department of Physics and Astronomy, Benedictine College, Atchison, Kansas, USA

3) Space Science and Engineering Division, Southwest Research Institute, San Antonio, Texas, USA

4) Johns Hopkins University Applied Physics Laboratory, Laurel, Maryland, USA

5) Institute for Astronomy and Space Physics, COCICET/University of Buenos Aires, Ciudad Universitaria, Buenos Aires, Argentina

6) Mullard Space Science Laboratory, University College London, Dorking, UK

7) Centre for Planetary Sciences, University College London/Birkbeck, London, UK

Key Points

1. Empirical production rates were derived for various superthermal electron fluxes
2. Electron and ion density discrepancies are not due to primary ion overproduction
3. Primary production is modeled without magnetospheric electron flux attenuation

Abstract

Ionization of neutrals by precipitating electrons and ions is the main source of Titan's nightside ionosphere. This paper has two goals: (1) characterization of the role of electron impact ionization on the nightside ionosphere for different magnetospheric conditions, and (2) presentation of empirical ion production rates determined using densities measured by the Cassini Ion and Neutral Mass Spectrometer (INMS) on the nightside. The ionosphere between 1000 and 1400 km is emphasized. We adopt electron fluxes measured by the Cassini Plasma Spectrometer Electron-Spectrometer and the Magnetospheric Imaging Instrument as classified by *Rymer et al.* [2009]. The current paper follows an earlier paper (Paper I), in which we investigated sources of Titan's dayside ionosphere and demonstrated that the photoionization process is well understood. The current paper (Paper II) demonstrates that modeled and empirical ionization rates on the nightside are in agreement with an electron precipitation source above 1100 km. Ion production rate profiles appropriate for different Saturnian magnetospheric conditions, as outlined by *Rymer et al*., are constructed for various magnetic field topologies. Empirical production rate profiles are generated for deep nightside flybys of Titan. The results also suggest that at lower altitudes (below 1100 km) another source, such as ion precipitation, is probably needed.

1 Introduction

As a result of ionization of its neutral atmosphere [*Waite et al.,* 2005, 2007; *Vuitton et al*., 2006, 2007; *Magee et al.,* 2009], Titan is surrounded by an ionosphere whose density peaks at altitudes between 900 and 1200 km [*Wahlund et al.,* 2005; *Young et al.,* 2005; *Keller et al.,* 1992; *Gan et al.,* 1992; *Cravens et al.,* 2004, 2005, 2008; 2009a,b; *Galand et al*., 1999;

43 *Banaskiewicz et al*., 2000; *Molina-Cuberos et al*., 2001; *Lilensten et al.,* 2005a, 2005b; *Agren et*
44 *al.,* 2007*; Kliore et al*., 2008; see recent review by *Galand et al*., 2014]. The ionosphere has
45 been detected using the radio occultation technique by both the Voyager 1 and Cassini spacecraft
46 [*Bird et al.,* 1997; *Kliore et al.,* 2008; *Cravens et al.,* 2009a]. In situ electron density
47 measurements were first made during the Cassini Ta encounter [*Wahlund et al.*, 2005] and ion
48 density measurements were first made by the Cassini Ion and Neutral Mass Spectrometer
49 (INMS) during the T5 nightside flyby of Titan [*Cravens et al.,* 2006].

50 Titan's location in Saturn's magnetosphere determines the superthermal electron
51 populations that exist and can precipitate along magnetic field lines into the ionosphere [*Carbary*
52 *and Krimigis*, 1982; *Arridge et al.,* 2006, 2008; *Coates et al*., 2007; *Carbary et al*., 2007;
53 *Bertucci et al.,* 2008; *Rymer et al*., 2009; *Sergis et al.*, 2009]. As, Titan lacks a significant
54 intrinsic magnetic field [*Hartle et al.,* 1982; *Neubauer et al.,* 1984], the magnetic field line
55 topology is dictated by the draping of Saturnian magnetic field lines around Titan [cf. review by
56 *Sittler et al.*, 2009]. *Rymer et al.* [2009] classified outer magnetospheric electron populations
57 based on Titan's location using data from the Cassini Plasma Science Electron Spectrograph
58 (CAPS ELS) and the Magnetospheric Imaging Instrument (MIMI). Four classes of spectra were
59 identified: (1) plasmasheet, (2) lobe-like, (3) magnetosheath, and (4) bi-modal. Related to this,
60 *Kliore et al.* [2011] emphasized the large variability in electron densities in Titan's ionosphere
61 measured by the Cassini Radio Science Subsystem indicating wide variations in the superthermal
62 electron population of the same classification.

63 Models of the ionosphere have shown that energetic magnetospheric electron and ion
64 precipitation can also take place and contribute to the ionization rate and atmospheric heating,
65 particularly at lower altitudes [cf. *Galand et al.,*2014; *Agren et al*., 2007; *Cravens et al.*,

2008;2009a,b; *Gronoff et al.*, 2009a,b; *Sillanpaa and Johnson, in press*]. Ionization sources on the nightside for the T5 encounter of Titan were discussed by *Agren et al.* [2007], *Cravens et al.* [2009b], *Robertson et al.* [2009], and *Gronoff et al.* [2009b]. One conclusion was that the flux of magnetospheric electrons precipitating into the atmosphere needs to be reduced by a factor of 10 in order to reproduce the electron densities measured by the RPWS-LP (Radio Plasma Wave Science-Langmuir Probe) instruments aboard the Cassini spacecraft. The current paper will come to different conclusions.

Snowden et al. [2013] and *Gan et al.* [1993] demonstrated that "erosion" of Saturnian magnetic flux tubes (i.e., depletion of the electron content) caught up in Titan's ionosphere can result in such attenuation of incident superthermal electron fluxes. *Gronoff et al.* [2009b] specifically examined the ion production of N_2^+, N^+ and CH_4^+ using their TransTitan model [*Gronoff et al.,* 2009a] in order to consider effects of magnetic field line geometry on the ionization processes. This was similar to the work done by *Cravens et al.* [2009b]. In situ magnetic field measurements [e.g., *Neubauer et al*., 1984; *Bertucci et al*., 2009] combined with post-Cassini global MHD and hybrid models [*Ma et al.* 2009; *Ledvina et al*., 2012] demonstrated that the magnetic field line topology is complex, particularly at lower altitudes. The magnetic fields produced by global models do not generally agree with magnetometer data below 1300 km or so [*Ulusen et al.,* 2010].

Chemical models incorporating neutral and/or ion chemistry have been created to explain observed ion densities at Titan [*Keller et al*., 1992; *Krasnopolsky*, 2009; *Lavvas et al*., 2008a; 2008b; *Robertson et al*., 2009; *Vuitton et al*., 2007, 2008; *Westlake et al.*, 2012; *Wilson and Atreya,* 2004]. *Robertson et al*. [2009] used a steady-state photochemical model of the ion-neutral chemistry that, coupled with a photoionization and two-stream code, generated the

primary (those caused by photoionization) and secondary (those caused by electron impact ionization) ion production rates and calculated ion densities as a function of altitude as was done in the model of *Keller et al*. [1992]. The model of *Robertson et al.* did not contain information about negative ion chemistry which could be important in the lower ionosphere [*Vuitton et al.,* 2008; *Agren et al.*, 2012; *Shebanits et al*., 2013; *Wellbrock et al.*, 2013; *Vigren et al.*, 2014] or ion transport effects which limit the applicability of this model above 1400 km, or to very long-lived ion species, where ion transport becomes non-negligible [*Ma et al*., 2006; *Cui et al*., 2010].

The current paper will use the two-stream method to handle suprathermal electron transport in the atmosphere. This method was originally used to calculate electron fluxes in the terrestrial ionosphere [*Nagy and Banks,* 1970] and has been used in models of both the energetics and composition of Titan's ionosphere [*Gan et al.,* 1992; *Cravens et al.,* 2009b; *Robertson et al.,* 2009; *Snowden et al.*, 2013]. This method derives from a gyrotropic distribution function averaged over a gyroperiod [cf. *Schunk and Nagy,* 2009]. As photoelectrons and magnetospheric electrons move along field lines they may scatter in a new direction or ionize a neutral thus creating another electron. This secondary electron must then also be tracked along the field line. Monte Carlo simulations have shown that considering only two streams, one up and one down [cf. *Schunk and Nagy,* 2009 and references therein] is usually sufficient in the ionosphere. Once "primary" ion production rates are determined (due to solar radiation, particle precipitation, etc.) chemistry alters the ion composition, as discussed in Paper I for the dayside.

First, comparisons between nightside INMS measurements and modeled ion densities will be made for a few passes (similar to what was done for the dayside in Paper I) [*Richard et al., in press*]. Empirical ion production rates will be constructed from INMS data using the methods of Paper I. Next, generic ion production profiles for the canonical cases discussed by

112 *Rymer et al.* [2009] will be generated for three magnetic field line topologies (horizontal
113 (nested), parabolic, and radial fields). The goal of this endeavor is to produce ion production rate
114 profiles to enable future modeling efforts to combine the solar ion production profiles with the
115 ion production caused by magnetospheric electrons when Titan is located in an area of Saturn's
116 magnetosphere characterized by *Rymer et al.* to predict the ion production and density profiles
117 for future flybys of Titan.

118 # 2 Methodology

119 Electron impact ionization appears to be the main in situ ionization source of the
120 nightside of Titan above ≈ 1000 km [cf. *Agren et al*., 2007; *Cravens et al*., 2009a,b; *Robertson et*
121 *al*., 2009]. In this section we provide more information on the methods used.

122 ## 2.1 Neutral Densities

123 The neutral densities required in the model are those measured by INMS for N_2, CH_4 and
124 H_2. Figure 4 shows densities for ingress of the T5 and T57 flybys. The densities all include a
125 factor of 3.15 increase associated with the recalibration of the instrument [cf. *Robertson et al.,*
126 2009; *Westlake et al.,* 2012; *Mandt et al.*, 2012]. Continuing calibration efforts [*Waite et al.,* in
127 preparation) indicate that the INMS closed source neutral density calibration factor might be
128 closer to 2.5 and that the factor for open source ion measurements might be a factor of 1.5 higher
129 than values used in this paper (which are consistent with *Mandt et al.*). As our empirical ion
130 production rates are obtained from the product of neutral and ion densities, the actual values
131 could potentially be 20% larger. This 20% modification is within statistical error bars of the data,
132 and the conclusions of the paper are unaffected.

133 Neutral densities for the remaining 35 neutral species in the model are determined using
134 the mixing ratio profiles of *Krasnopolsky* [2009], or *Lavvas et al.* [2011] for the case of CH_2NH,
135 anchored to mixing ratios reported by *Magee et al.* [2009], *Cui et al.* [2009], and *Robertson et al.*
136 [2009]. This method is described in detail in Paper I [*Richard et al., in press*]

137 Another set of neutral density profiles were used in our determination of "generic" ion
138 production rates associated with precipitation of different magnetospheric electron populations as
139 outlined by *Rymer et al.* [2009]. The global average model of the neutral atmosphere discussed
140 in Paper I [*Richard et al*.] was implemented and was based on INMS [*Magee et al.,* 2009] data
141 from 40 Titan flybys and on the Huygens Atmospheric Structure Instrument (HASI) data below
142 960 km [*Fulchignoni et al.,* 2005], from which profiles of N_2, CH_4 and H_2 are derived (Figure 4).

143 **2.2 Two-Stream Equations for Suprathermal Electron Flux**

144 Electron fluxes as a function of energy and ion production rates are calculated by solving
145 two-stream equations [*Nagy and Banks,* 1970; *Schunk and Nagy,* 2009] using Saturn's
146 magnetospheric electron flux (i.e., Figure 1). Discussion of the application of this method to
147 Titan can be found in *Gan et al*. [1992, 1993], *Cravens et al*. [2009b], and *Richard et al.* [2011].
148 Given the complexity of the magnetic field topology and at least partial disagreement of global
149 plasma/field models (e.g., MHD) with magnetometer data, we follow the lead of *Gan et al*. and
150 adopt parabolic field lines in addition to radial field lines. The apex altitude determines the dip
151 angle of the field lines at ionospheric altitudes. For example, for T5 putting the apex at the
152 surface results in field lines that have a dip angle of about 45° near 1100 km, in agreement with
153 Cassini magnetometer data shown by *Richard et al.* [2011] and discussed in *Cravens et al.*

154 2009b]. These papers show that the magnetic field vectors have large radial and horizontal
155 components throughout the T5 flyby. Parabolic field lines are shown in Figure 2.

156 We now briefly describe how the inelastic electron impact cross sections, σ, for a species
157 j with an electron of energy E are calculated using the parametric formula of *Green and Dutta*
158 [1967]. For the differential ionization cross section the expression developed by *Green and*
159 *Sawada* [1972] is implemented. Elastic electron differential cross sections are calculated from
160 the values of *Trajmar et al*. [1983] and *Solomon et al.* [1988] and have been integrated by *Gan et*
161 *al.* [1992] in order to obtain the backscatter probabilities and the elastic cross section as a
162 function of energy for electron-N_2 collisions. The sum of vibrational excitations of molecular
163 nitrogen through inelastic collisions was taken from *Porter et al.* [1976]. For the cross section of
164 the A, B, B', W, C, a, a' and W states the revised cross sections of *Cartwright et al.* [1977] by
165 *Trajmar et al.* [1983] were used. The cross sections of the b' and $^1\Pi_u$ were obtained from *Zipf*
166 *and McLaughlin* [1978]. The sum of the Rydberg states was derived by normalizing the values
167 from *Green and Stolarski* [1972] to the total dissociation cross sections of *Zipf and McLaughlin*
168 when they are added to the cross sections of the b' and $^1\Pi_u$ states.

169 The ionization cross sections of *Tabata et al.* [2006] and *Itikawa* [2006] are used in the
170 current work. Differential elastic electron-impact cross sections of methane have been taken
171 from the theoretical work of *Jain* [1986] over energy ranges from 0.1–1 eV, 2.5-20 eV, and 30–
172 400 eV. Backscattering probabilities, integrated cross sections and momentum transfer cross
173 sections have been calculated from these results. The results of *Tanaka et al.* [1983] are used
174 for the differential cross sections above 2 eV. Measurements are provided between 3 and 20 eV,
175 and extrapolations are used for energies above 20 eV. Vibrational excitation cross sections at 2

176 eV are taken from those of *Rohr* [1980], and for energies below 2 eV cross sections are used
177 from the measurements of *Sohn et al.* [1983].

178 The electronic excitation cross sections of methane are derived from the measurements of
179 *Vuskovic and Trajmar* [1983]. Rotational excitation cross sections for methane are taken from
180 the theoretical work of *Jain and Thompson* [1983] and multiplied by a factor of 2 in order to
181 bring their work into better agreement with measurements of *Muller et al.* [1985], *Brescansin et*
182 *al.* [1989], and *Shimamura* [1983]. Ionization cross sections for CH_4 are taken from the work of
183 *Straub et al.* [1997] as revised by *Lindsay and Mangan* [2003] and reviewed by *Liu and*
184 *Shemansky* [2006].

185 The 2-stream equations require the downward flux at the upper boundary. We use a
186 variety of downward electron fluxes based on magnetospheric electron fluxes measured by
187 Cassini in the nearby Saturnian magnetosphere. For example, in modeling electron precipitation
188 for T5, *Cravens et al*. [2009b] used the CAPS ELS fluxes which are reproduced here in Figure 3
189 with a factor of 3.15 increase in the neutral densities to account for INMS recalibration. Also
190 shown are the CAPS ELS electron fluxes measured at 1200 km, near the ionospheric peak, and
191 our calculated fluxes are within 5-20% of the CAPS ELS fluxes up to energies of 200 eV using
192 parabolic magnetic field lines anchored at the surface of Titan (Figure 2). Between 200 and
193 1000 eV the CAPS-ELS data is at the one count level which is the statistical error bound of the
194 instrument and our model differs from these fluxes by as much as a factor of 2 which could be
195 the result of modest attenuation of the electron fluxes [*Snowden et al.,* 2013]. The CAPS-ELS
196 instrument was pointed in the ram direction and as a result the pitch angle of the instrument was
197 approximately 90˚ [cf. *Cravens et al.,* 2009b].

2.3 Ion Chemistry and Empirical Modeling

The photochemical model we use here was described in Paper I [*Richard et al., in press*], and was derived from the earlier photochemical models of *Keller et al.* [1992, 1998], *Cravens et al.* [2004], and *Robertson et al.* [2009]. This time-independent model does not include ion transport between altitudes or horizontal locations as a result of bulk plasma flow, an assumption valid below ≈ 1350 km [*Ma et al*., 2006, 2009; *Cravens et al.,* 2010]. In addition to adopting the primary ion production rates the model includes a large number of ion-neutral and electron-ion dissociative recombination chemical reactions. Reaction rate coefficients are taken from *Keller et al.* [1992, 1998], *Anicich* [2003], *Anicich and McEwan* [1997], *Cravens et al*. [2005], *Vuitton et al.* [2006, 2007], *McEwan and Anicich* [2007], *Edwards et al.* [2008], *Zabka et al*. [2009], *Robertson et al*. [2009], and *Westlake et al.* [2012]. We use 10 km intervals between 725 and 2715 km but only show results below about 1700 km.

As discussed in Paper I [*Richard et al.*], a measured density of N_2^+ cannot be determined by INMS ion measurements because $HCNH^+$ is a more abundant mass 28 species due to ion-neutral chemistry. The overwhelming majority of N_2^+ on the nightside is produced by electron impact ionization and about 60-85% of this N_2^+ is lost via chemical reactions with methane, producing CH_3^+. A small amount of CH_3^+ is produced by dissociative ionization of methane. Roughly 90-99% of the CH_3^+ is lost via reaction with methane to produce CH_4^+. Thus, the production of CH_3^+ serves as a good indicator (or proxy) of the primary production of N_2^+.

CH_3^+ densities from the model are compared with the densities measured by INMS in Figure 5. This illustrates that the production rate of N_2^+ (the major source of CH_3^+) in the model is reasonable. The drop in ion densities near 1200 km will be discussed later. In the companion Paper 1, an empirical production rate of N_2^+ was derived from densities of CH_3^+ and CH_4

measured by INMS by means of a simple two-reaction model and the assumption of photochemical equilibrium (which is valid below ≈1350 [*Ma et al*., 2006, 2009; *Cravens et al*., 2010]). The main loss process for CH_3^+ is through reaction with methane. Not quite all of N_2^+ reacts with CH_4 to produce CH_3^+, so the full photochemical model was used to derive a branching ratio of CH_3^+ produced to the total amount of N_2^+ produced (Figure 6). This ratio only varies about 20% over the extent of the ionosphere. Using this model-derived branching ratio, the derived empirical production rate (reasonable to within 40%) of N_2^+ determined by setting the production rate of N_2^+ equal to the loss rate from the reaction between CH_3^+ and CH_4 is given by:

$$Production_{N_2^+} = \frac{k_{CH_3^+,CH_4}[CH_3^+]_{INMS}[CH_4]_{INMS}}{Branching\ Ratio} \quad (1)$$

Similarly, an empirical primary production rate of CH_4^+ due to ionization of CH_4 can be derived. Note that about 90% of the CH_4^+ loss is due to reaction with methane to produce CH_5^+, but that other sources (besides primary ionization) exist (e.g., CH_4 reacting with H_2^+, H^+ or N^+). Therefore, this production rate is the loss rate of CH_4^+ (via reaction with CH_4) modified by a branching ratio (Figure 6) to account for alternative production pathways (see Paper I [*Richard et al.*]). The empirical primary production rate (including the model-derived branching ratio) is:

$$Production_{CH_4^+} = \frac{k_{CH_4^+,CH_4}[CH_4]_{INMS}[CH_4^+]_{INMS}}{Branching\ Ratio} \quad (2)$$

3 Verification of Nightside Ion Production Rates via Simple Empirical Methods

In this section, the model ionization rates (from electron impact) are compared with the empirical production rates, just as was done in Paper 1 for solar radiation. We start with data

from the T5 flyby, as this case has been previously discussed in the literature (i.e., *Cravens et al.,* [2009b], *Robertson et al.* [2009], *Gronoff et al.* [2009b], and *Agren et al*. [2007]), and then we discuss the T57 flyby. For the T5 case, Titan was in the plasmasheet and T57 corresponds to what *Rymer et al*. [2009] call "bimodal" magnetospheric electron distributions. We find that overall the model production rates of the primary ion species are in reasonable agreement with the production rates derived from INMS density measurements, as will be discussed below for the canonical cases of *Rymer et al.* (lobe-like, plasmasheet, bimodal, and magnetosheath) and for three magnetic field line topologies (radial, single parabola, nested parabolas simulating horizontal field lines).

3.1 T5 – Plasmasheet Electron Populations

The T5 flyby of Titan occurred on the deep nightside of Titan and the Cassini Orbiter reached a closest approach altitude of 1027 km where the solar zenith angle was 137º. The neutral density profiles we used to analyze this pass were shown in Figure 4. A parabolic magnetic field line anchored at the surface generates a field line dip angle in agreement with magnetometer data between 1000 and 1400 km [*Ulusen et al.,* 2010; *Backes et al*., 2005; *Cravens et al*., 2010; *Ma et al*., 2009]. The magnetospheric electron fluxes used as inputs for this case were discussed earlier (i.e., the plasmasheet case shown in Figure 3).

Figure 5 shows the CH_3^+ densities produced by the full photochemical model, and the model CH_3^+ densities are in good agreement with densities measured by INMS to within 20% for altitudes below 1160 km and above 1280 km. Between 1160 and 1275 km INMS and modeled CH_3^+ densities differ by about a factor of 2. This feature was noticed by both *Agren et al.* [2007] and *Cravens et al.* [2009b]. *Cravens et al.* demonstrated that the CAPS ELS 4 eV electron flux,

corresponding to secondary electrons, correlates well with the INMS density of CH_5^+, the product of the chemical reaction between CH_4^+ and methane, with a noticeable dip between 155 and 205 seconds after closest approach corresponding to altitudes of 1140 and 1220 km respectively. *Cravens et al.* also noted that the density profiles of longer-lived ions (such as $HCNH^+$) do not exhibit such a profound drop in density at these altitudes. As the drop in density was only prevalent in shorter-lived ion species, *Cravens et al.* concluded that the production rate of ions, and hence the magnetospheric electron flux at the end of the flux tube connected to this region, was passing through more of the neutral atmosphere and was being depleted of its electron content [*Gronoff et al.*, 2009b; *Snowden et al.*, 2013]. This effect has been noted in several previous works [*Gan et al.,* 1992*; Agren et al.,* 2007; *Cravens et al.,* 2009b; *Ma et al.,* 2006, 2009; *Snowden et al.,* 2013]. *Cui et al*. [2010] suggested that transport from the dayside can also contribute to the densities of long-lived ions on the nightside.

Although some depletion of the incident electron flux is apparently needed near 1200 km as discussed in *Gan et al.* [1992], and *Snowden et al.*[2013], at other altitudes the model agrees very well with INMS data. This indicates that overall for T5, the magnetospheric electron flux tube content appears to be depleted less than originally thought. This has significant consequences for our understanding of the Titan interaction with Saturn's magnetosphere. Earlier modelers (*Agren et al.* [2007] and *Cravens et al.* [2009b]) concluded otherwise, due to a recent recalibration of the neutral density profile and a focus on modeled total ion and electron densities which were too high. As will be shown below, our current model also produces electron densities that are too high, but we think the explanation (as discussed in Paper 1) is missing loss processes for major ion species (but not for CH_3^+), just as occurs on the dayside. This will be discussed further later in the paper.

Next, we use CH_3^+ and CH_4 densities measured by INMS to obtain empirical N_2^+ production rates (methods discussed earlier and in Paper 1), which are shown in Figure 7 and compared with the two-stream model with the full T5 CAPS ELS magnetospheric electron fluxes as input. The agreement between this model and the CAPS ELS measurement and the model of *Gronoff et al.* [2009b] for their radial field line with attenuation is within 10 – 20% near the ionospheric peak with the exception of the "bite-out" feature between 1140 and 1220 km. At higher altitudes the discrepancy between our model and the model of *Gronoff et al.* increases due to our use of a parabolic instead of radial field line. This in conjunction with the agreement between modeled and measured CH_3^+ densities suggests that the two-stream model is producing adequate amounts of N_2^+ for the measured inputs.

The above methods were also applied to T5 for CH_4 ionization producing CH_4^+. Figure 8 shows the CH_4^+ densities from the full model compared with INMS densities. Again the agreement is good overall, but the "bite-out" is not reproduced by the model. Empirical ion production rates derived from INMS data are shown in Figure 9.

CH_4^+ production rates modeled using only magnetospheric electron impact ionization with the two-stream code and those derived empirically from INMS data agree between 1350 and 1200 km but are a factor of two lower between 1150 and 1000 km. However, this model's production rate is found to be in agreement with the radial case presented by *Gronoff et al.* [2009b] with a value of 0.04 $cm^{-3}s^{-1}$ between 1100 and 1000 km.

3.2 T57- Bimodal Electron Populations

The T57 flyby of Titan occurred on June 22, 2009, and the spacecraft reached a closest approach altitude of 955 km. During the inbound leg the solar zenith angle went from 165˚ at an

310 altitude of nearly 2000 km to 128˚ at closest approach, indicating that this is an entirely nightside
311 situation. *Rymer et al.* [2009] classified the magnetospheric electron flux for this pass as a
312 bimodal case (Figure 10).

313 For T57 we compare our calculated electron fluxes with fluxes measured by CAPS-ELS
314 anode 2 at several altitudes and for different model cases (Figure 11). Results from several
315 CAPS-ELS anodes (i.e., different directions) are shown. Note that anodes 3-6 point into the ram
316 direction and see negative grains as well as electrons, so we will not comment on these. Anode 7
317 also appears to show negative ion contamination so we compare our results with measurements
318 made by anode 2. Throughout the flyby the CAPS pitch angle was near 90˚ as was the case for
319 the T5 flyby.

320 Only the more energetic electrons can reach 995 km, although locally-produced
321 secondary electrons at low energies (0 - 30 eV) are also present. At 10 eV the 725 km case
322 fluxes agree with CAPS ELS better than the surface parabola model fluxes (which are too large).
323 For energies between about 20 eV - 300 eV the model fluxes agree with agree better with the
324 CAPS data than the 725 km parabola results, which are too low by a factor of 2 or so. At 1064
325 km both model cases compare well with data, although model fluxes are somewhat too high
326 fluxes near 5 - 10 eV and too low for energies above 1 keV (though the CAPS fluxes are close to
327 the 1-count level there). But the more draped 725 km magnetic field parabola gives somewhat
328 better agreement overall. At 1163 km and higher for T57, both models agree rather well with the
329 measured fluxes, although are maybe somewhat too large for energies greater than 1 keV or so.

330

Magnetometer data (Figure 11) shows [*Bertucci et al*., 2009; *Simon et al*., 2010; *Luhmann et al*., 2012] that the magnetic field line topology for T57 has both radial and horizontal (parallel to the surface of Titan) components near the ionospheric peak and then becomes more horizontal as altitude increases. Near closest approach, the magnetic field exhibits the strongest radial components. We ran the model with three different magnetic field line topologies (nested, single parabola anchored at the surface, single parabola anchored at 725 km). The nested case represents completely horizontal field lines at all altitudes "sampled." The parabola anchored at the surface has field lines with a 45˚ angle with respect to Titan near 1200 km and the parabolic anchored at 725 km has a larger horizontal field component near 1200 km.

The CH_3^+ density profile produced by the full photochemical model with the surface-anchored parabolic field line agrees best with the measured INMS density profile between 1130 and 1350 km (Figure 12). In particular, the peak CH_3^+ densities agree well. But below 1100 km, better agreement with data is obtained with a parabolic magnetic field line anchored at 725 km (that is, more horizontal, or highly draped, magnetic field). As the magnetometer observed more larger radial components of the magnetic field near closest approach (Figure 11) this could indicate a modest attenuation. Overall, the model generates reasonable primary ionization rates (i.e., N_2^+ production rates) and, unlike *Cravens et al*. [2009b], *Gronoff et al.* [2009b] or *Agren et al*. [2007] for T5, without requiring attenuation of the magnetospheric electron fluxes from their full magnetospheric values.

Figure 13 shows the empirical N_2^+ production rate derived from CH_3^+ and CH_4 densities measured by INMS for T57. For comparison, the production rate from the full model is shown for the surface-anchored and 725 km-anchored parabolae cases.

353 Primary production of CH_4^+ from electron impact ionization of methane was also
354 calculated for T57. Again, the modeled and INMS measured densities of CH_4^+ agree best for the
355 surface anchored parabola case above 1150 km and the 725 km-anchored parabola case below
356 1140 km. The modeled densities of CH_4^+ are within 20% of the measured values. Figure 14
357 shows the empirical primary CH_4^+ production rates derived from densities of CH_4^+ and CH_4
358 measured by INMS.

359 **3.3 Generic Nightside Ion Production Rates for Different Inputs**

360 In this section the full 2-stream plus chemical model is used to generate ion production
361 rate profiles for all 4 "Rymer cases" [*Rymer et al.,* 2009] for the magnetospheric electron
362 populations and for all the magnetic field configurations. The global average neutral density
363 model presented in Paper 1 is used. No attenuation of magnetospheric electron fluxes is
364 assumed. The cases shown are for: (1) lobe-like from the T8 flyby, (2) plasmasheet from the
365 T13 flyby, (3) bimodal from the T31 flyby, and (4) magnetosheath from the T32 flyby. The
366 results are shown in Figure 14 for N_2^+ production and in Figure 15 for CH_4^+ production resulting
367 from electron-impact ionization. Table 1 shows relative production rates of the other ion species
368 produced by electron impact, so that the results of Figures 15 and 16 can be extended to other
369 "primary" ion species. Note that these ratios are rather insensitive to electron energies above
370 about 20-30 eV or so (Table 1) as these energies are above the ionization threshold for these
371 products.

372 Figures 15 and 16 illustrate that in general higher energy electrons penetrate deeper into
373 the ionosphere generating ion production at lower altitudes. This is why the lobe-like,
374 plasmasheet, and bimodal electron flux cases produce production rate profiles peaking at lower

375 altitudes in comparison with the lower energy electrons from the magnetosheath. Higher energy
376 electrons also produce secondary electrons that can generate further ionization and, obviously,
377 higher incident electron fluxes result in higher ion production rates.

378 As illustrated earlier for T5 and T57, the magnetic field line topology is also important in
379 determining where incident electrons will deposit their energy [cf. *Galand et al.*, 2010; *Gronoff*
380 *et al.*, 2009b; *Robertson et al.,* 2009; *Richard et al.*, 2011]. In general, the nested magnetic field
381 line case, horizontal magnetic field lines, produces peak production rates 8-10 times lower than
382 the parabola anchored at 725 km and 20-30 times lower than the radial magnetic field line. The
383 peak altitude of the production rates generated with the nested magnetic field line is between
384 approximately 150 (200) km higher than the peak altitude obtained with the parabolic magnetic
385 field line anchored at 725 km (radial magnetic field line) for the lobe, bimodal, and plasmasheet
386 case and 200 (300) km higher for the magnetosheath case. These results are to be expected as
387 the lower energy electrons more readily impact the neutral ions, and thus the flux will decay
388 more rapidly than that of a higher energy electron population moving through the same amount
389 of atmosphere. Jagged peaks appear in radial cases in Figure 15. This is an artifact of the model
390 resolution as the radial field line model has a resolution of 35 km where the nested and parabolic
391 magnetic field line geometries have 10 km-altitude resolution.

392 The shapes of the production rate profiles of CH_4^+ are similar to those of N_2^+ (Figure 16).
393 The production rate profiles generated in this section can be used in conjunction with the
394 production rate profiles for the solar cases in order to create generic ion production profiles for a
395 variety of solar zenith angles and magnetospheric electron conditions.

3.4 Empirical Production Rates for Other Nightside Flybys

Other than T5 and T57, other nightside Titan flybys we examined with INMS ion and neutral data suitable for obtaining empirical ion production rates are T26, T32, T36, T50, and T51. The N_2^+ empirical production rates, organized according to plasmasheet, lobe-like and bimodal nightside flybys, are shown in Figure 17 using Equation (1) and an adjustment factor of 0.67 from Paper I [*Richard et al., in press.*] and Figure 6 in the current paper to account for the amount of N_2^+ that does not react to form CH_3^+. Only deep nightside flybys containing INMS data are included which is why there is not a curve for the lobe-like electron flux. The error bars represent the uncertainties in the production rates associated with the measured CH_3^+ and CH_4 densities. Comparison of Figures 15 and 17 confirms that the modeled electron precipitation reasonably represents the empirical production rates in shape and magnitude, however for the plasmasheet and magnetosheath cases, radial field line topology must be used. Also, the theoretical electron-impact production rates are falling short of the empirical production rates below altitudes of about 1050 km. Perhaps there is a missing, non-electron precipitation, ionization source such as energetic ion precipitation [e.g., *Cravens et al.,* 2008; *Edberg et al.*, 2013; *Sillanpaa and Johnson*, in press] or ion transport from the dayside for the case of longer-lived ions [*Cui et al*., 2010].

4 Discussion

The model N_2^+ production rates agree well with the empirical INMS production rates for the surface parabola case for the T5 flyby at all altitudes except between 1175 - 1300 km, where model production rates exceed empirical rates by a factor of 2 - 3. The surface parabola magnetic field configuration gives a magnetic field orientation that agrees with Cassini

418 magnetometer data. Figure 18 shows our electron-impact-based model results for $HCNH^+$,
419 $C_2H_5^+$, and the thermal electron density for T5. Just as on the dayside, the modeled densities of
420 these major species are too high, even though the primary production rates are fine, leading to
421 the conclusion that the model is missing chemical sinks. Similar comparisons for other flybys
422 (e.g., T57) lead to the same conclusions.

423 For T57, the agreement of our model N_2^+ production rates with the INMS empirical
424 production rates is good above an altitude of 1125 km, particularly with the surface parabola
425 magnetic field model (i.e., the less-draped magnetic field). But the surface parabola model ion
426 production rates become a factor of 2 too large below 1125 km, and the 725 km parabola model
427 (more draped field lines) provides better agreement.

428 For T57, the orientation of the measured magnetic field agrees overall with the surface
429 parabola for higher altitudes. However, at lower altitudes measured field has a large component,
430 whereas the better field-model for production rate comparison is the more highly-draped field,
431 which is puzzling.

432

433 As we discussed earlier in the paper, *Cravens et al.,* [2009b] and *Agren et al.* [2007]
434 assumed that the boundary electron fluxes into the electron transport model had to be reduced
435 from fluxes in the outer magnetosphere by a factor of ≈ 10 in order to bring model electron
436 densities into agreement with electron densities measured by the RPWS-LP or total ion density
437 measured by INMS. As discussed earlier the suggestion was made than this attenuation is due
438 the electron content of a magnetic flux tube in Saturn's magnetosphere being depleted over time
439 as it is "hung up" in Titan's ionosphere (cf. *Gan et al.*, 1992; *Snowden et al.*, 2013). However,

440 in the intervening time period, INMS neutral densities have increased by a factor of 2 - 3
441 (*Robertson et al.,* 2009; *Westlake et al.,* 2012; *Mandt et al.*, 2012), affecting the model energy
442 deposition, and there has been a growing recognition (*Galand et al*., 2014; *Westlake et al*., 2012;
443 *Richard et al*., 2014) that photochemical models of Titan's ionosphere are missing loss processes
444 for higher mass ion species.

445 The current paper's nightside ionosphere empirical ion production rate determinations
446 (from INMS primary ion species) and model calculations indicate that factor of 10
447 magnetospheric electron flux attenuation is no longer needed. However, for the time period (or
448 locations) on the outbound T5 pass, when Cassini was in the 1175 - 1300 km altitude range, a
449 factor of 2-3 lower boundary electron flux reduction appears to be required, suggesting that at
450 least for those flux tubes attenuation/depletion could be taking place. For T57, lower
451 suprathermal electron fluxes below 1125 km altitude would give better model -data agreement.
452 The model runs show that a more draped magnetic field configuration could accomplish this, but
453 the measured magnetic field below 1125 km (Figure 11) is actually more radial (i.e., less
454 draped), indicating that a factor of 2-3 electron flux attenuation is probably necessary for that
455 time period (or location on Titan). It should be noted that negative ions also contribute to the
456 overall charge density of the ionosphere [*Coates et al.*, 2007; *Agren et al*., 2012; *Shebanits et al.*,
457 2013; *Wellbrock et al.*, 2013; *Vigren et al.*, 2014].

458 Model-data comparisons in the current paper indicate that attenuation is not needed
459 overall. If a major attenuation is no longer needed the problem then becomes how to explain the
460 overabundance of electrons in the models. An interesting feature in the ion densities measured
461 by INMS during T5, first pointed out by *Cravens et al*. [2009b], has some bearing on this issue
462 as mentioned earlier in the current paper (see the discussion in section 3.1). That is, the

empirical production rates do show that in some locations there must be lower magnetospheric electron fluxes, perhaps due to the aforementioned attenuation. However, the chemically longer-lived species (e.g., $HCNH^+$) show smoother profiles than do the primary species (Figure 18), indicating that time history of a flux tube is also important and also indicating that transport of ionospheric plasma from the dayside could be playing a role [*Cui et al.,* 2010]. More work is needed on this topic.

5 Conclusions

In conclusion, the key findings of this study are:

1. Theoretically modeled electron-ion production rates are found to be within 25% of production rates derived empirically from INMS measurements for the T5 and T57 nightside flyby of Titan.
2. The cause of the discrepancy between modeled and measured (data taken by INMS, RSS, and RPWS-LP) electron and ion densities is not due to overproduction of the primary ion species and therefore must be caused by insufficient electron-ion recombination.
3. Attenuation of the magnetospheric electron fluxes to the extent proposed by *Agren et al.* [2007] and *Cravens et al.* [2009b] is not needed to reproduce the primary production rates of the primary ion species on the nightside of Titan, although *Snowden et al.* [2013] have shown that flux tube erosion can lower ionization rates below 1300 km. If there is a large attenuation to the electron flux additional ionization sources (i.e. ion precipitation) may be responsible.
4. Globally averaged ion production profiles have been generated for the ionization products of N_2 and CH_4 resulting from magnetospheric electron precipitation using the

magnetospheric electron conditions described by *Rymer et al.* [2009] for a radial, a nested, and a parabolic magnetic field line anchored at 725 km. These production rates can be combined with the solar zenith angle dependent production rates shown in Paper I to account for various conditions of Titan's ionosphere.

5. Empirical production rates have been derived from INMS measurements on the nightside of Titan for the plasmasheet, bimodal, and magnetosheath superthermal electron fluxes. These indicate that electron precipitation from the external plasma environment can account for most of the nightside ionosphere (and perhaps make a contribution on the dayside ionosphere, although it would be hard to observe due to large solar photoionization rates). However, our results show that below 1050 km or so, ionization by another source (i.e., ion precipitation) might be needed and that transport of plasma from the dayside could also be important for longer-lived ion species [cf. *Cui et al*., 2010].

Acknowledgements. All Cassini data, including INMS data, is or will soon be available through the Planetary Data System. The research described in this paper was supported at the University of Kansas by NASA Cassini grant NA57-03001 via subcontract from the Southwest Research Institute and by NASA Planetary Atmospheres grant NNX10AB86G.

References

Agren, K., and 15 colleagues (2007), On magnetospheric electron impact ionization and dynamics in Titan's ram-side and polar ionosphere—A Cassini case study, *Ann. Geophys., 25*, 2359–2369.

Ågren, K., N. J. T. Edberg, and J.-E. Wahlund (2012), Detection of negative ions in the deep ionosphere of Titan during the Cassini T70 flyby, *Geophys. Res. Lett*., *39*, L10201, doi:10.1029/2012GL051714.

Anicich, V. (2003), An index of the literature for bimolecular gas phase cation-molecule reaction kinetics, *JPL Publication,* 03-19.

Anicich, V., and M. McEwan (1997), Ion-molecule chemistry in Titan's ionosphere, *Planet. Space Sci., 45*(8), 897-921.

Arridge, C. S., N. Achilleos, M. K. Dougherty, K. K. Khurana, and C. T. Russell (2006), Modeling the size and shape of Saturn's magnetopause with variable dynamic pressure, *J. Geophys. Res., 111*, A11227, doi:10.1029/2005JA011574.

Arridge, C. S., N. Andre´, N. Achilleos, K. K. Khurana, C. L. Bertucci, L. K. Gilbert, G. R. Lewis, A. J. Coates, and M. K. Dougherty (2008), Thermal electron periodicities at 20RS in Saturn's magnetosphere, *Geophys. Res. Lett., 35*, L15107, doi:10.1029/2008GL034132.

Backes, H., F. M. Neubauer, M. K. Dougherty, H. Achilleos, N. Andre, C. S. Arridge, C. Bertucci, G. H. Jones, and K. K. Khurana (2005), Titan's magnetic field signature during the first Cassini encounter, *Science, 308*, 992–995.

525 Banaskiewicz, M., L. M. Lara, R. Rodrigo, J. J. Lopez-Moreno, and G. J. Molina-Cuberos
526 (2000), A coupled model of Titan's atmosphere and ionosphere, *Icarus, 147*, 386– 404.

527 Bertucci, C., et al. (2008), The magnetic memory of Titan's ionized atmosphere, *Science, 321*,
528 1475–1478, doi:10.1126/science.1159780.

529 Bertucci, C., N. B. Sinclair, N. Achilleos, P. Hunt, M. K. Dougherty, and C. S. Arridge (2009),
530 The variability of Titan's magnetic environment, *Planet. Space Sci. 57*, 1813-1820,
531 doi:10.1016/j.pss.2009.02.009.

532 Bird, M. K., R. Dutta-Roy, S. W. Asmar, and T. A. Rebold (1997), Detection of Titan's
533 ionosphere from Voyager 1 radio occultation observations, *Icarus, 130*, 426–436.

534 Brescansin, L. M., M. A. P. Lima, and V. Mckoy (1989), Cross sections for rotational excitation
535 of CH_4 by 3-20 eV electrons, *Phys. Rev. A, 40*, no. 10, 5577.

536 Carbary, J. F., and S. M. Krimigis (1982), Charged particle periodicity in the Saturnian
537 magnetosphere, *Geophys. Res. Lett., 9*, 1073 – 1076, doi:10.1029/GL009i009p01073.

538 Carbary, J. F., D. G. Mitchell, S. M. Krimigis, D. C. Hamilton, and N. Krupp (2007), Charged
539 particle periodicities in Saturn's outer magnetosphere, *J. Geophys. Res., 112*, A06246,
540 doi:10.1029/2007JA012351.

541 Cartwright, D. C., S. Trajmar, A. Chutjian, and W. Williams (1977), Electron impact excitation
542 of the electronic states of N2. II Integral cross sections at incident energies from 10 to 50
543 eV, *Phys. Rev. A, 16* 1041.

544 Coates, A. J., F. J. Crary, D. T. Young, K. Szego, C. S. Arridge, Z. Bebesi, and E. C. Sittler Jr.
545 (2007), Ionospheric electrons in Titan's tail: Plasma structure during the Cassini T9
546 encounter, *Geophys. Res. Lett,. 34*, L24505–L24519, doi:10.1029/ 2007GL030919.

547 Cravens, T. E., J. Vann, J. Clark, J. Yu, C. N. Keller, and C. Brull (2004), The ionosphere of
548 Titan: An updated theoretical model, *Adv. Space Res, 33*, 212–215.

549 Cravens, T. E., and 15 colleagues (2005), Titan's ionosphere: Model comparisons with Cassini
550 Ta data, *Geophys. Res. Lett., 32 (12)*, L12108, doi:10.1029/2005GL023249.

551 Cravens, T., I. Robertson, J. Waite Jr., R. Yelle, W. Kasprzak, C. Keller, S. Ledvina, H.
552 Niemann, J. Luhmann, R. McNutt, et al. (2006), Composition of Titan's ionosphere,
553 *Geophys. Res. Lett.*, *33* (7), L07,105.

554 Cravens, T. E., I. P. Robertson, S. A. Ledvina, D. Mitchell, S. M. Krimigis, and J. H. Waite Jr.
555 (2008), Energetic ion precipitation at Titan, *Geophys. Res. Lett., 35*, 03103. doi:10.1029/
556 2007GL032451.

557 Cravens, T. E., R. V. Yelle, J.-E. Wahlund, D. E. Shemansky, and A. F. Nagy (2009a),
558 Composition and structure of the ionosphere and thermosphere. In: *Titan from Cassini-*
559 *Huygens*. edited by R. H. Brown, J.-P. Lebreton, and J. H. Waite Jr., Springer, New York,
560 pp. 259–296.

561 Cravens, T. E., et al. (2009b), Model–data comparisons for Titan's nightside ionosphere, *Icarus,*
562 *199*, 174.

563 Cravens, T. E., et al. (2010), Dynamical and magnetic field time constants for Titan's ionosphere:
564 Empirical estimates and comparisons with Venus, *J. Geophys. Res.*, *115*, A08319,
565 doi:10.1029/2009JA015050.

566 Cui, J., R. V. Yelle, V. Vuitton, J. H. Waite, Jr., W. T. Kasprzak, D. A. Gell, H. B. Niemann, I.
567 C. F. Müller-Wodarg, N. Borggren, G. G. Fletcher, E. L. Patrick, E. Raaen, and B. Magee
568 (2009), Analysis of Titan's neutral upper atmosphere from Cassini Ion Neutral Mass
569 Spectrometer measurements, *Icarus*, *200*, 581.

570 Cui, J., M. Galand, R. V. Yelle, J.-E. Wahlund, K. Ågren, J. H. Waite Jr., and M. K. Dougherty
571 (2010), Ion transport in Titan's upper atmosphere, *J. Geophys. Res., 115*, A06314,
572 doi:10.1029/2009JA014563.].

573 Edberg, N. J. T., et al. (2013). Extreme densities in Titan's ionosphere during the T85
574 magnetosheath encounter, *Geophys. Res. Lett*., *40*, 2879-2883, doi:10.1002/grl.50579.

575 Edwards, S., C. Freeman, and M. McEwan (2008), The ion chemistry of methylenimine and
576 propionitrile and their relevance to Titan, *Int. J. Mass Spectrom., 272*(1), 86–90.

577 Fulchignoni, M., et al. (2005), In situ measurements of the physical characteristics of Titan's
578 environment, *Nature, 438,* 785-791.

579 Galand, M., J. Lilensten, D. Toublanc, and S. Maurice (1999), The ionosphere of Titan: Ideal
580 diurnal and nocturnal cases, *Icarus, 140*, 92–105.

581 Galand M., R. Yelle, J. Cui, J.-E. Wahlund, V. Vuitton, A. Wellbrock, and A. Coates
582 (2010), Ionization sources in Titan's deep ionosphere, *J. Geophys. Res.*, *115*, A07312,
583 doi: 10.1029/2009JA015100.

584 Galand, M., A. Coates, T. Cravens, and J.-E. Wahlund (2014), Titan's Ionosphere, in *Titan:*
585 *Interior, Surface, Atmosphere, and Space Environment*, edited by I. C. F. Mueller-
586 Wodarg, C. A. Griffith, E. Lellouch, and T. E. Cravens, pp. 376-418, Cambridge
587 University Press, New York, ISBN: 0521199921.

588 Gan, L., C. N. Keller, and T. E. Cravens (1992), Electrons in the ionosphere of Titan, *J. Geo-*
589 *phys. Res., 97*, 12136–12151

590 Gan, L., T. E. Cravens, and C. N. Keller (1993), A time-dependent model of suprathermal
591 electrons at Titan. In: Gombosi, T. I. (Ed.) *Plasma Environments of Non-Magnetic*
592 *Planets*, vol. 4, p. 171, Elsevier.

593 Green, A. E. S., and S. K. Dutta (1967), Semi-empirical cross sections for electron impacts, *J.*
594 *Geophsys. Res., 72,* 3933.

595 Green, A. E. S., and T. Sawada (1972), Ionization cross sections and secondary electron
596 distributions, *J. Atmos. Terr. Phys., 34*, 1719.

597 Green, A. E. S., and R. S. Stolarski (1972), Analytic models of electron impact excitation cross
598 sections, *J. Atmos. Terr. Phys., 34,* 1703-1717.

599 Gronoff, G., J. Lilensten, L. deSorgher, and E. Fluckiger (2009a), Ionization processes in the
600 atmosphere of Titan I. Ionization in the whole atmosphere, *Astron. Astrophys., 506*, 955-
601 964.

602 Gronoff, G., J. Lilensten, and R. Modolo (2009b), Ionization processes in the atmosphere of
603 Titan II. Electron precipitation along magnetic field lines, *Astron. Astrophys., 506*, 965-
604 970.

605 Hartle, R. E., E. C. Sittler, Jr., K. Ogilvie, J. D. Scudder, A. J. Lazarus, and S. K. Atreya (1982),
606 Titan's ion exosphere observed from Voyager 1, *J. Geophys. Res., 87*, 1383.

607 Itikawa, I. (2006), Cross sections for electron collisions with nitrogen molecules, *J. Phys. Chem.*
608 *Ref. Data*, *35*, 31-53.

609 Jain, A. (1986), Total (elastic + absorption) cross sections for e-CH_4 collisions in a spherical
610 model at 0.10-500 eV, *Phys. Rev. A, 34*, no. 5, 3707.

611 Jain, A., and D. G. Thompson (1983), Rotational excitation of CH_4 and H_2O by slow electron
612 impact, *J. Phys. B: Atom. Mol. Phys., 16*, 3077.

613 Keller, C. N., T. E. Cravens, and L. Gan (1992), A model of the ionosphere of Titan, *J. Geophys.*
614 *Res., 97*, 12117–12135.

615 Keller, C. N., V. G. Anicich, and T. E. Cravens (1998), Model of Titan's ionosphere with
616 detailed hydrocarbon chemistry, *Planet. Space Sci., 46*, 1157–1174.

617 Kliore, A. J., and 12 colleagues (2008), First results from the Cassini radio occultations of the
618 Titan ionosphere, *J. Geophys. Res., 113*, A09317, doi:10.1029/2007JA012965.

619 Kliore, A. .J., A. F. Nagy, T. E. Cravens, M. S. Richard, and A. M. Rymer (2011), Unusual
620 electron density profiles observed by Cassini radio occultations in Titan's ionosphere:
621 Effects of enhanced magnetospheric electron precipitation? *J. Geophys. Res., 116*,
622 A016694, doi:10.1029/2011JA016694.

623 Krasnopolsky, V. (2009), A photochemical model of Titan's atmosphere and ionosphere. *Icarus,*
624 *201*, 226-256.

625 Lavvas, P. P., A. Coustenis, and I. M. Vardavas, (2008a), Coupling photochemistry with haze
626 formation in Titan's atmosphere. Part I. Model description, *Planet. Space Sci., 56*, 27–66.

627 Lavvas, P. P., A. Coustenis, and I. M. Vardavas, (2008b), Coupling photochemistry with haze
628 formation in Titan's atmosphere. Part II. Results and validation with Cassini/Huygens
629 data, *Planet. Space Sci., 56*, 67–99.

630 Lavvas, P., M. Galand, R. V. Yelle, A. N. Heays, B. R. Lewis, G. R. Lewis, and A. J. Coates
631 (2011), Energy deposition and primary chemical products in Titan's upper atmosphere,
632 *Icarus*, *213*, 233-251, doi:10.1016/j.icarus.2011.03.001.

633 Ledvina, S. A., S. H. Brecht, and T. E. Cravens (2012), The orientation of Titan's dayside
634 ionosphere and its effects on Titan's plasma interaction, *Earth, Planets and Space, 64,*
635 doi:10.5047/eps.2011.08.009.

636 Lilensten, J., O. Witasse, C. Simon, H. Soldi-Lose, O. Dutuit, R. Thissen, and C. Alcaraz
637 (2005a), Prediction of a N++ 2 layer in the upper atmosphere of Titan, *Geophys. Res.*
638 *Lett., 32*, L03203, doi:10.1029/2004GL021432.

639 Lilensten, J., C. Simon, O. Witasse, O. Dutuit, R. Thissen, and C. Alcarez (2005b), A fast
640 comparison of the diurnal secondary ion production in the ionosphere of Titan, *Icarus,*
641 *174*, 285–288.

642 Lindsay, B. G., and M. A. Mangan (2003), Cross sections for ion production by electron
643 collision with molecules, in *Landolt-Börnstein, Photon- and Electron-Interaction With*
644 *Molecules: Ionization and Dissociation, New. Ser.,* vol. I/17C, edited by Y. Itikawa, pp.
645 5-1- 5-77, Springer, New York.

646 Liu, X., and D. E. Shemansky (2006), Analysis of electron impact ionization properties of
647 methane, *J. Geophys. Res.*, 111, A04303-A04319.

648 Luhmann, J., et al. (2012), Investigating magnetospheric interaction effects on Titan's
649 ionosphere with the Cassini orbiter Ion Neutral Mass Spectrometer, Langmuir Probe and
650 magnetometer observations during targeted flybys, *Icarus, 219,* 534-555,
651 doi:10.1016/j.icarus.2012.03.015.

652 Ma, Y., A. F. Nagy, T. E. Cravens, I. V. Sokolov, K. C. Hansen, J.-E. Wahlund, F. J. Crary, A. J.
653 Coates, and M. K. Dougherty (2006), Comparisons between MHD model calculations
654 and observations of Cassini flybys of Titan, *J. Geophys. Res., 111*, A05207,
655 doi:10.1029/2005JA011481.

656 Ma, Y.-J., et al. (2009), Time-dependent global MHD simulations of Cassini T32 flyby: From
657 magnetosphere to magnetosheath. *J. Geophys. Res., 114*, A03204,
658 doi:10.1029/2008JA013676.

659 Magee, B., J. Bell, J. H. Waite Jr., K. Mandt, J. Westlake, and D. Gell (2009), INMS derived
660 composition of Titan's upper atmosphere: Analysis methods and model comparison,
661 *Planet. Space Sci., 57*, 1895-1916.

662 Mandt, K. E., and 18 colleagues (2012), Ion densities and composition of Titan's upper
663 atmosphere derived from the Cassini Ion Neutral Mass Spectrometer: Analysis methods
664 and comparison of measured ion densities to photochemical model simulations, *J.*
665 *Geophys. Res., 117*, E10006, doi: 10.1029/2012JE004139.

McEwan, M. J., and V. G. Anicich (2007), Titan's ion chemistry: A laboratory perspective, *Mass Spectrom. Rev. 26*, 281–319.

Molina-Cuberos, G. J., H. Lammer, W. Stumptner, K. Schwingenschuh, H. O. Rucker, J. J. Lopez-Moreno, K. Rodrigo, and T. Tokano (2001), Ionosphere layer induced by meteoric ionization in Titan's atmosphere, *Planet. Space Sci., 49*, 143–153.

Muller, R., K. Jung, K.-H. Kochem, W. Sohn, and H. Ehrhardt (1985), Rotational excitation of CH_4 by low-energy-electron collisions, *J. Phys. B: Atom. Mol. Phys., 18,* 3971.

Nagy, A. F., and P. M. Banks (1970), Photoelectron fluxes in the ionosphere, *J. Geophys. Res., 75*, 6260–6270.

Neubauer, F. M., D. A. Gurnett, J. D. Scudder, and R. E. Hartle (1984), Titan's magnetospheric interaction. In *Saturn*, edited by T. Gehrels and M. D. Matthews, Univ. of Arizona Press, Tucson, pp. 760–787.

Porter, H. S., C. H. Jackman, and A. E. S. Green (1976), Efficiencies for production of atomic nitrogen and oxygen by relativistic proton impact in air, *J. Chem. Phys., 65*, 154.

Richard, M. S., T. E. Cravens, I. P. Robertson, J. H. Waite, J.-E. Wahlund, F. J. Crary, and A. J. Coates (2011), Energetics of Titan's ionosphere: Model comparisons with Cassini data, *J. Geophys. Res*., *116*, A09310,doi:10.1029/2011JA016603.

Richard, M. S., T. E. Cravens, C. Wylie, D. Webb, Q. Chediak, R. Perryman, K. Mandt, J. Westlake, J. H. Waite Jr., I. Robertson, B. A. Magee and N. J. T. Edberg (in press), An empirical approach to modeling ion production rates in Titan's ionosphere I: Ion production rates on the dayside and globally, DOI: 10.1002/2013JA019706

687 Robertson, I. P., T. E. Cravens, J. H. Waite Jr., R. V. Yelle, V. Vuitton, A. J. Coates, J.-E.
688 Wahlund, K. Agren, K. Mandt, B. Magee, and M.S. Richard (2009), Structure of Titan's
689 ionosphere: Model comparisons with Cassini data., *Planet. Space Sci., 57*, 1834,
690 doi:10.1016/j.pss.2009.07.011.

691 Rohr, K. (1980), Cross beam experiment for the scattering of low-energy electrons from
692 methane, *J. Phys. B: Atom. Mol. Phys., 13*, 4897.

693 Rymer, A. M., H. T. Smith, A. Wellbrock, A. J. Coates, and D. T. Young (2009), Discrete
694 classification and electron energy spectra of Titan's varied magnetospheric environment,
695 *Geophys. Res. Lett., 36,* L15109, doi:10.1029/2009GL039427.

696 Schunk, R. W., and A. F. Nagy (2009), *Ionospheres, Second Edition*. Cambridge Univ. Press,
697 Cambridge.

698 Sergis, N., S. M. Krimigis, D. G. Mitchell, D. C. Hamilton, N. Krupp, B. H. Mauk, E. C. Roelof,
699 and M. K. Dougherty, (2009), Energetic particle pressure in Saturn's magnetosphere
700 measured with the Magnetospheric Imaging Instrument on Cassini, *J. Geophys. Res*.,
701 *114*, A02214, doi:10.1029/2008JA013774.

702 Shebanits, O., J.-E. Wahlund, K. Mandt, K. Ågren, N. J. T. Edberg, and J. H. Waite Jr. (2013),
703 Negative ion densities in the ionosphere of Titan-–Cassini RPWS/LP results, *Planet.*
704 *Space Sci., 84*, 153-162, doi:10.1016/j.pss.2013.05.021.

705 Shimamura, I. (1983), Partial-sum rules for and asymmetry between rotational transitions J±ΔJ
706 ← J. *Phys. Rev. A, 28,* no. 3, 1357.

707 Sillanpaa, I., and R. Johnson (in press), The role of ion-neutral collisions in Titan's
708 magnetospheric interaction, *J. Geophys. Res.*

709 Simon, S., U. Motschmann, G. Kleindienst, J. Saur, C. L. Bertucci, M. K. Dougherty, C. S.
710 Arridge, and A. J. Coates (2009), Titan's plasma environment during a magnetosheath
711 excursion: Real-time scenarios for Cassin's T32 flyby from a hybrid simulation, *Ann.*
712 *Geophys.*, *27*, 669–685.

713 Sittler, E. C., R. E. Hartle, C. Bertucci, A. Coates, T. E. Cravens, I. Dandouras, and D. E.
714 Shemansky (2009), Energy deposition processes in Titan's upper atmosphere and its
715 induced magnetosphere. In *Titan from Cassini-Huygens*, edited by R. H. Brown, J.-P.
716 Lebreton, and J. H. Waite, Springer, New York, pp. 393-454.

717 Snowden, D., R. V. Yelle, M. Galand, A. J. Coates, A. Wellbrock, G. H. Jones, and P. Lavvas,
718 (2013), Auroral electron precipitation and flux tube erosion in Titan's upper atmosphere,
719 *Icarus*, *226*(1), 186-204.

720 Sohn, W., K. Jung, and H. Ehrhardt (1983), Threshold structures in the cross section of low-
721 energy electron scattering of methane, *J. Phys. B: Atom. Mol. Phys., 16*, 891.

722 Solomon, S. C., P. B. Hays, and V. J. Abreu (1988), The auroral 6300Å emission: Observations
723 and modeling, *J. Geophys. Res., 93*, 9867.

724 Straub, H. C., D. Lin, B. G. Lindsay, K. A. Smith, and R. F. Stebbings (1997), Absolute partial
725 cross sections for electron-impact ionization of CH_4 from threshold to 1000 eV, *J. Chem.*
726 *Phys.,106,* 4430-4435.

727 Tabata, T., T. Shirai, M. Sataka, and H. Kubo (2006), Analytic cross sections for electron impact
728 collisions with nitrogen molecules, *Atomic Data Nucl. Data Tabl.*, *92*, 375-406.

729 Tanaka, H., M. Kubo, N. Onodera, and A. Suzuki (1983), Vibrational excitation of CH_4 by
730 electron impact: 3-20 eV, *J. Phys. B: Atom. Mol. Phys., 16*, 2861.

731 Trajmar, S., D. F. Register, and A. Chutjian (1983), Electron scattering by molecules II.
732 Experimental methods and data, *Physics Reports (Review Section of Physics Letters), 97*,
733 219.

734 Ulusen., D., J. G. Luhmann, Y.-J. Ma, S. Ledvina, T. E. Cravens, K. Mandt, J. H. Waite, and J.-
735 E. Wahlund (2010), Investigation of the force balance in the Titan ionosphere: Cassini T5
736 flyby model/data comparisons, *Icarus, 210*, 867-880, doi: 10.1016/j.icarus.2010.07.004.

737 Vigren, E., M. Galand, O. Shebanits, J.-E. Wahlund, W.D. Geppert, P. Lavvas, V. Vuitton, and
738 R.V. Yelle (2014), Increasing positive ion number densities below the peak of ion-
739 electron pair production in Titan's ionosphere, *Astrophs J*, *786*, 69, doi:10.1088/0004-
740 637X/786/1/1.

741 Vuitton, V., R. V. Yelle, and V. G. Anicich (2006), The nitrogen chemistry of Titan's upper
742 atmosphere revealed, *Astrophys. J., 647*, L175–L178.

743 Vuitton, V., R. V. Yelle, and M. McEwan (2007), Ion chemistry and N-containing molecules in
744 Titan's upper atmosphere, *Icarus, 191*, 722–742.

745 Vuitton, V., R. Yelle, and J. Cui (2008), Formation and distribution of benzene on Titan, *J.*
746 *Geophys. Res.*, *113* (E5), E05,007.

747 Vuskovic, L., and S. Trajmar (1983), Electron impact excitation of methane, *J. Chem. Phys., 78*,
748 4947.

749 Wahlund, J.-E., and 17 colleagues (2005), Cassini measurements of cold plasma in the
750 ionosphere of Titan, *Science, 308*, 986–989.

751 Waite Jr., J. H., and 21 colleagues (2005), Ion Neutral Mass Spectrometer (INMS) results from
752 the first flyby of Titan, *Science, 308*, 982–986.

753 Waite Jr., J. H., D. T. Young, T. E. Cravens, A. J. Coates, F. J. Crary, B. Magee, and J. Westlake
754 (2007), The process of tholin formation in Titan's upper atmosphere, *Science, 316*, 870–
755 875.

756 Wellbrock, A., A. J. Coates, G. H. Jones, G. R. Lewis, and J. H. Waite (2013), Cassini CAPS-
757 ELS observations of negative ions in Titan's ionosphere: Trends of density with altitude,
758 *Geophys. Res. Lett., 40*, 4481–4485, doi:10.1002/grl.50751.

759 Westlake, J. H., J. H. Waite Jr., K. E. Mandt, N. Carrasco, J. M. Bell, B. A. Magee, and J.-E.
760 Wahlund (2012), Titan's ionospheric composition and structure: Photochemical modeling
761 of Cassini INMS data, *J. Geophys. Res., 117*, E01003, doi:10.1029/2011JE003883.

762 Wilson, E., and S. Atreya (2004), Current state of modeling the photochemistry of Titan's
763 mutually dependent atmosphere and ionosphere, *J. Geophys. Res.*, *109*, E06,002.

764 Young, D. T., and 42 colleagues (2005), Composition and dynamics of plasma in Saturn's
765 magnetosphere, *Science, 307*, 1262–1266.

766 Zabka, J., M. Polasek, D. Ascenzi, P. Tosi, and D. Schroder (2009), Reactivity of $C_2H_5^+$ with
767 benzene: Formation of ethylbenzenium ions and implications for Titan's ionospheric
768 chemistry, *J. Phys. Chem. A, 113*(42), 11,153-11,160.

769 Zipf, E. C., and R. W. McLaughlin (1978), On the dissociation of nitrogen by electron impact
770 and by E.U.V. photo-absorption, *Planet. Space Sci., 26*, 449.

771

Table and Figure Captions

Table 1: Ratios of minor ion primary production rate to major ion primary production rate at the ionospheric peak due to electron impact.

Figure 1: Superthermal electron fluxes measured by the Cassini CAPS and MIMI instruments in Saturn's outer magnetosphere plotted against energy for the four magnetospheric plasma environments presented by *Rymer et al.* [2009].

Figure 2: Parabolic magnetic field line topology used in the model. The apex altitude of each field line is indicated on the graph.

Figure 3: Suprathermal magnetospheric electron fluxes measured by CAPS during the T5 encounter as reported by *Cravens et al.* [2008] at 1200 km (above) and 2730 km (below). The downward flux comes from suprathermal electron transport along the field line from the magnetosphere to the ionosphere. These CAPS ELS fluxes for T5 were adopted as the boundary condition for the two-stream code, and model fluxes are also shown. The upward electron fluxes appearing at higher energies are calculated from the model and are the result of backscattering, and at lower energies are escaping secondary electrons produced by ionization deeper in the atmosphere.

Figure 4: Number density of major neutral species derived from INMS measurements for the global average (solid lines), T5 (dashed lines), and T57 (dotted lines) flyby of Titan. N_2, CH_4 and H_2 are indicated by the black, red and blue line, respectively. The number densities have been multiplied by a factor of 3.15 in this figure in order to account for a potential recalibration of the INMS instrument.

Figure 5: CH_3^+ density produced by the full photochemical model (green triangles) using the full T5 magnetospheric electron flux measured by CAPS ELS [*Cravens et al.*, 2008] as an input (Figure 3) compared to INMS data from the T5-Outbound flyby of Titan. INMS data is indicated with the blue diamonds. This model uses the magnetic field topology of a single parabola anchored at the surface of Titan to simulate a curved field line with a large radial component.

Figure 6: Branching ratio used to adjust the production rate of N_2^+ and CH_4^+ derived from the simple two-reaction model using INMS data for the outbound leg of the T5 and T57 flybys. This is the ratio of the production rate of CH_3^+ to N_2^+ (below) and of the primary production of CH_4^+ to the total production of CH_4^+ from the full photochemical model (above).

Figure 7: Modeled electron impact production rates of N_2^+ (green triangles) compared to the production rate of N_2^+ derived from INMS data using a simple two – reaction model adjusted by dividing the loss rate of CH_3^+ via reaction with methane by the branching ratio shown in Figure 6 (blue diamonds) for the outbound leg of the T5 flyby of Titan. The modeled production rates of *Gronoff et al*. [2009b] for a radial field line with flux attenuation are also shown (red dashes). A single parabolic field line anchored at the surface of Titan is used for the magnetic field line topology.

Figure 8: CH_4^+ density produced with the full photochemical model (green triangles) compared to INMS data (blue diamonds) from the T5-Outbound flyby of Titan. A single parabolic field line anchored at the surface of Titan is used for the magnetic field line topology.

Figure 9: Shown here are modeled production rates (green triangles) of CH_4^+ compared to the empirical production rate of CH_4^+ derived from INMS data (blue diamonds) using the simple

two-reaction chemical model for the T5-Outbound flyby of Titan and adjusted by dividing the loss rate of CH_4^+ via reaction with methane by the branching ratio shown in Figure 6. The modeled production rates of *Gronoff et al*. [2009b] for a radial field line with flux attenuation are also shown (red dashes).

Figure 10: Comparisons between modeled electron fluxes and those measured by CAPS during the T57 encounter at 995 km (top), 1290 km (middle) and 1619 km(bottom). Measurements taken by CAPS-ELS anode 2 are shown in red, modeled fluxes up (black) and down (blue) are shown for parabolic field lines anchored at 725 km (solid) and the surface of Titan (dashed). The CAPS-ELS one count level is shown with a green line.

Figure 11: Magnetometer data taken by the MAG instrument aboard Cassini during the T57 flyby. Magnetic field components in TIIS coordinates are shown (top) as well as the ratio of the radial component to the total magnitude of the magnetic field (bottom).

Figure 12: CH_3^+ density produced by the full photochemical model with magnetic field line topologies of a parabola anchored at the surface of Titan (green triangles), a parabola anchored at 725 km (purple crosses) and nested parabola (red stars) using the T57 magnetospheric electron flux measured by CAPS ELS [*Kliore et al.*, 2011] as an input (Figure 10) compared to INMS data from the T57-Outbound flyby of Titan. INMS data is indicated with the blue diamonds. Note that although the surface-anchored parabola is more favored above 1100 km, the 725 km parabola appears to give better agreement below that altitude.

834 **Figure 13:** Modeled photoionization production rates of N_2^+ with magnetic field line
835 topologies of a parabola anchored at the surface of Titan (green triangles), a parabola anchored at
836 725 km (purple crosses) and nested parabola (red stars) compared to the production rate of N_2^+
837 derived from INMS data using a simple two – reaction model adjusted by dividing the loss rate
838 of CH_3^+ via reaction with methane by the branching factor shown in Figure 6 (blue diamonds)
839 for the inbound leg of the T57 flyby of Titan.

840 **Figure 14:** Modeled production rates of CH_4^+ with magnetic field line topologies of a parabola
841 anchored at the surface of Titan (green triangles), a parabola anchored at 725 km (purple crosses)
842 and nested parabola (red stars) using the full photochemical model compared to the empirical
843 production rate of CH_4^+ derived from INMS data (blue diamonds) calculated by dividing the loss
844 rate of CH_4^+ via reaction with methane by the branching ratio shown in Figure 6 for the T57-
845 Inbound flyby of Titan.

846 **Figure 15:** Production of N_2^+ using nested (dotted grey), parabolic (dashed) and radial
847 (solid) magnetic field lines and the magnetospheric electron fluxes of the *Rymer et al.*
848 [2009] classifications. Results are shown for model runs using the T8 lobe-like, T13
849 plasmasheet, T31 bimodal and the T32 magnetosheath electron fluxes measured by
850 CAPS/ELS. The magnetospheric electron flux profiles are shown in Figure 1.

851 **Figure 16:** Primary production of CH_4^+ using nested (dotted grey), parabolic (dashed), and
852 radial (black) magnetic field lines and the magnetospheric electron fluxes of the *Rymer et al.*
853 [2009] classifications. Results are shown for model runs using the T8 lobe-like, the T13
854 plasmasheet, the T31 bimodal, and the T32 magnetosheath electron fluxes measured by CAPS
855 ELS. The magnetospheric electron flux profiles are shown in Figure 1.

856 **Figure 17:** Empirical production rates for N_2^+ derived using the simple two-reaction model
857 (Equation 1), INMS measured densities and an adjustment factor of 0.67. Production rates are
858 generated for nightside flybys classified as plasmasheet (top), magnetosheath (middle) and
859 bimodal (bottom) electron fluxes. Error bars represent uncertainties in INMS measured
860 densities.

861 **Figure 18**: Comparisons between RPWS-LP measured (blue diamonds) and modeled electron
862 densities (blue line) and INMS measured (lines) and modeled densities of $HCNH^+$ (green
863 triangles) and $C_2H_5^+$ (red squares).

864

865 **Table 1: Ratios of minor ion primary production rate to major ion primary**
866 **production rate at the ionospheric peak due to electron impact.**

Flyby	Altitude [km]	N^+ to N_2^+	CH_3^+ to CH_4^+	CH_2^+ to CH_4^+	CH^+ to CH_4^+	H_2^+ to CH_4^+	H^+ to CH_4^+
T8	1045	0.262	0.758	0.124	0.055	0.080	0.126
T13	1025	0.228	0.765	0.141	0.066	0.056	0.156
T31	1045	0.257	0.758	0.125	0.055	0.080	0.128
T32	1355	0.155	0.748	0.134	0.061	0.088	0.118

867

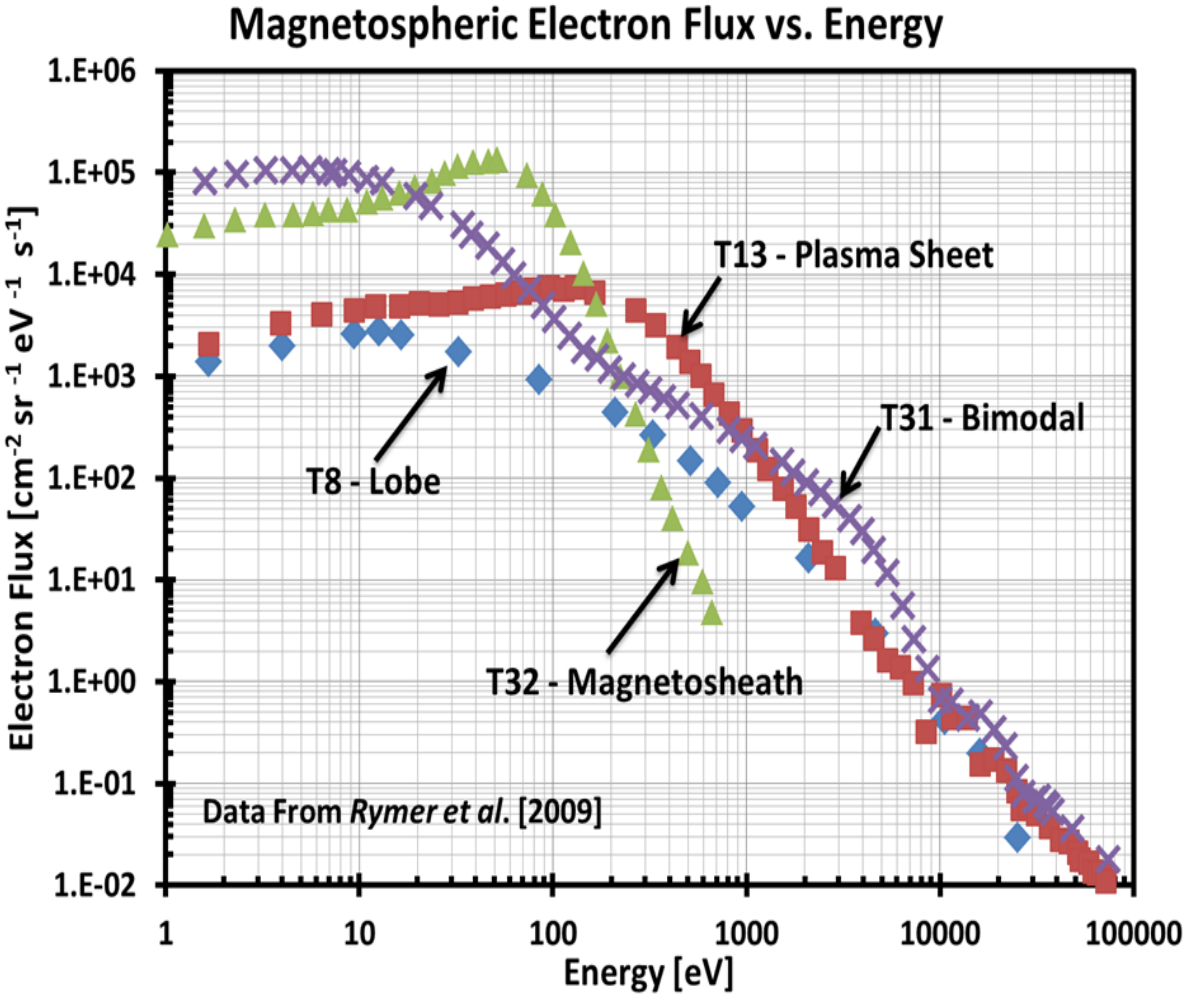

Figure 1: Superthermal electron fluxes measured by the Cassini CAPS and MIMI instruments in Saturn's outer magnetosphere plotted against energy for the four magnetospheric plasma environments presented by *Rymer et al.* [2009].

868

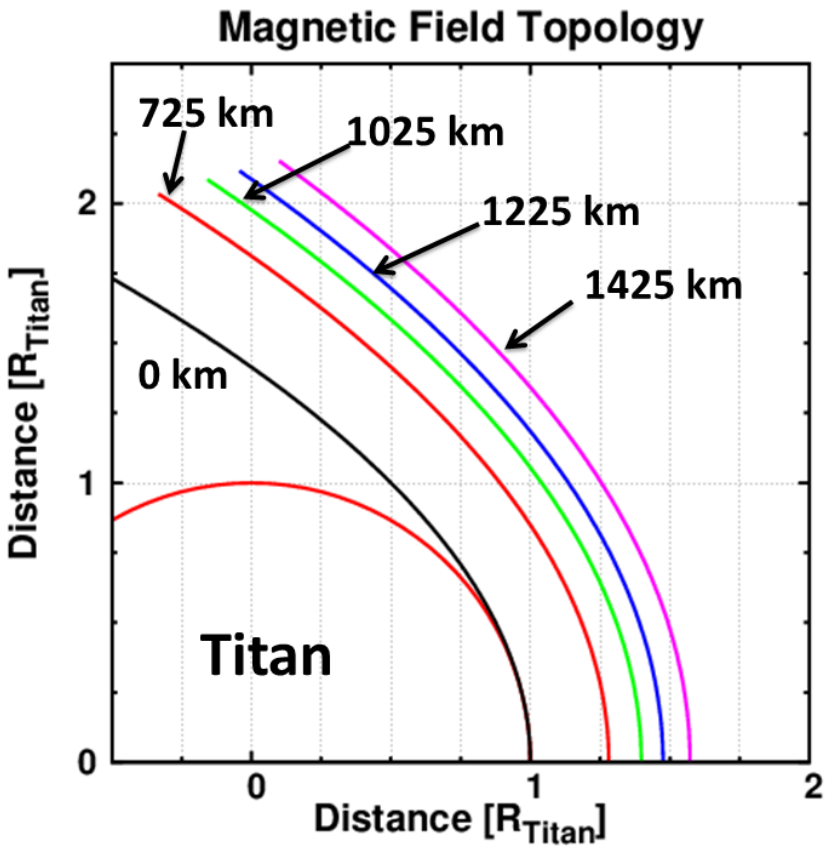

Figure 2: Parabolic magnetic field line topology used in the model. The apex altitude of each field line is indicated on the graph.

869

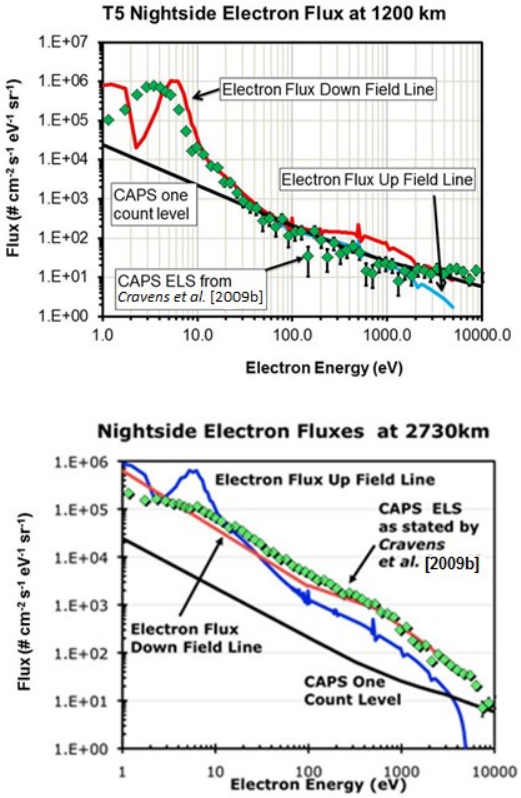

Figure 3: Suprathermal magnetospheric electron fluxes measured by CAPS during the T5 encounter as reported by *Cravens et al.* [2009b] at 1200 km (above) and 2730 km (below). The downward flux comes from suprathermal electron transport along the field line from the magnetosphere to the ionosphere. These CAPS ELS fluxes for T5 were adopted as the boundary condition for the two-stream code, and model fluxes are also shown. The upward electron fluxes appearing at higher energies are calculated from the model and are the result of backscattering, and at lower energies are escaping secondary electrons produced by ionization deeper in the atmosphere.

870

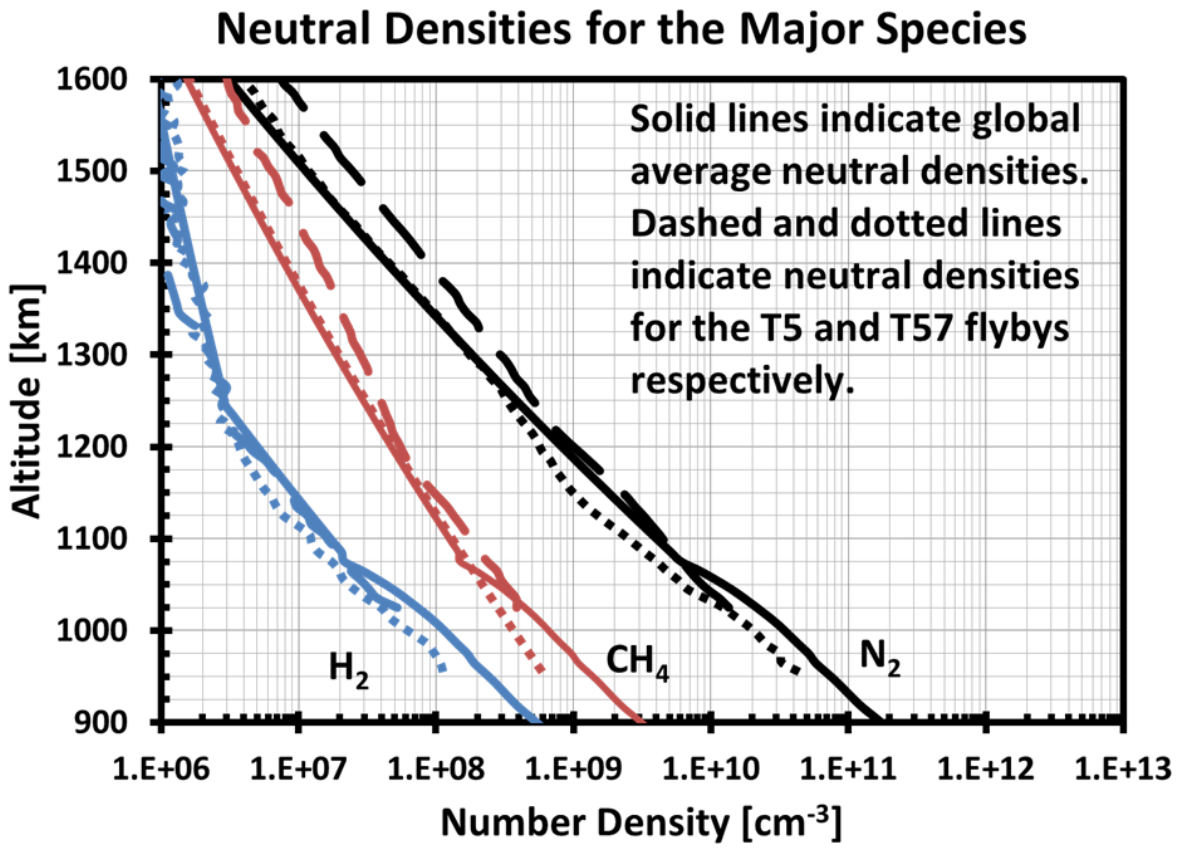

Figure 4: Number density of major neutral species derived from INMS measurements for the global average (solid lines), T5 (dashed lines), and T57 (dotted lines) flyby of Titan. N_2, CH_4 and H_2 are indicated by the black, red and blue line, respectively. The number densities have been multiplied by a factor of 3.15 in this figure in order to account for a potential recalibration of the INMS instrument.

871

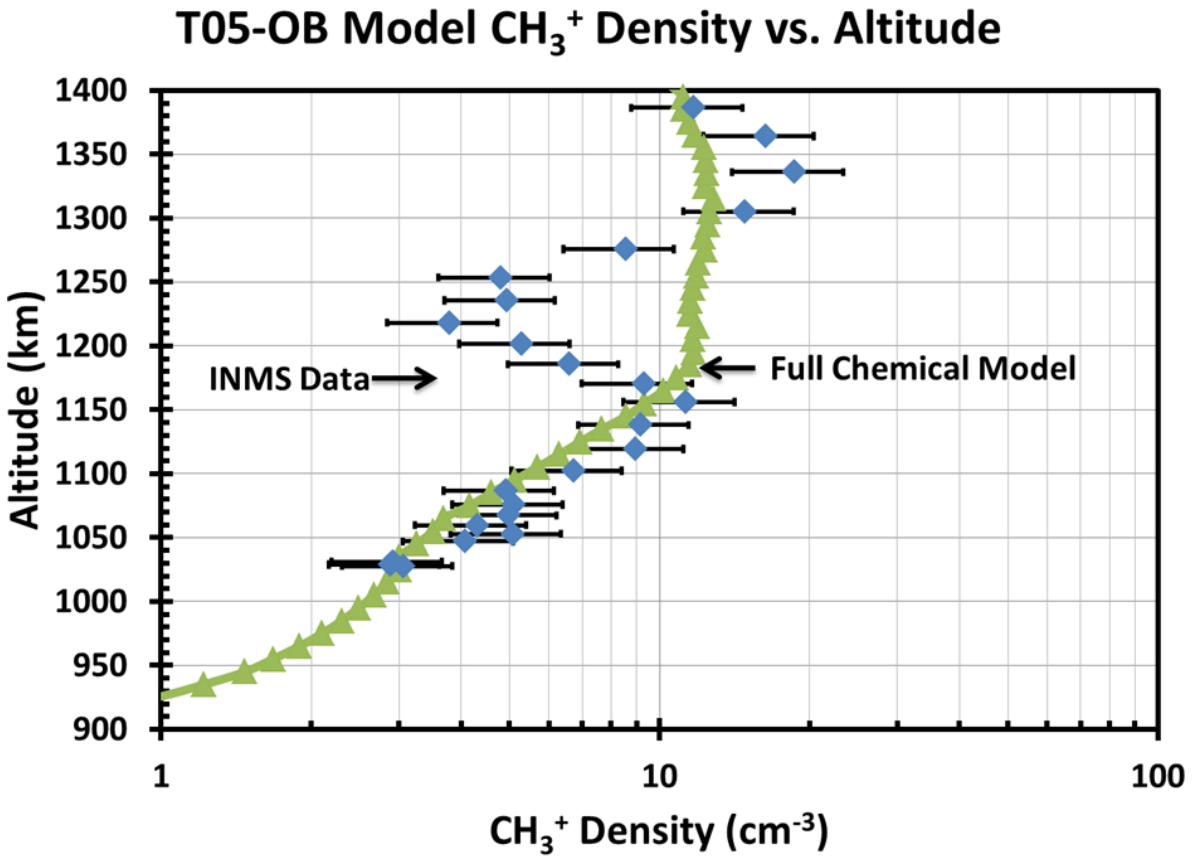

Figure 5: CH_3^+ density produced by the full photochemical model (green triangles) using the full T5 magnetospheric electron flux measured by CAPS ELS [*Cravens et al.*, 2008] as an input (Figure 3) compared to INMS data from the T5-Outbound flyby of Titan. INMS data is indicated with the blue diamonds. This model uses the magnetic field topology of a single parabola anchored at the surface of Titan to simulate a curved field line with a large radial component.

872

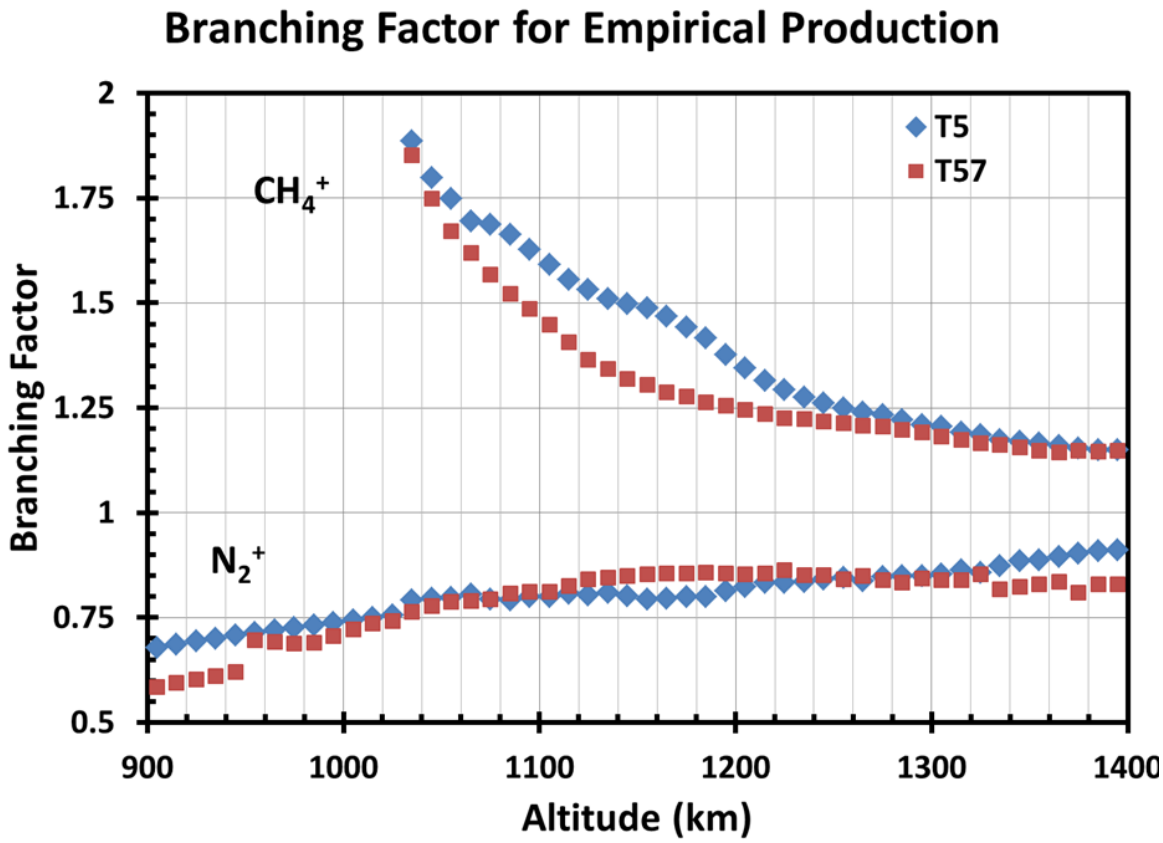

Figure 6: Branching ratio used to adjust the production rate of N_2^+ and CH_4^+ derived from the simple two-reaction model using INMS data for the outbound leg of the T5 and T57 flybys. This is the ratio of the production rate of CH_3^+ to N_2^+ (below) and of the primary production of CH_4^+ to the total production of CH_4^+ from the full photochemical model (above).

873

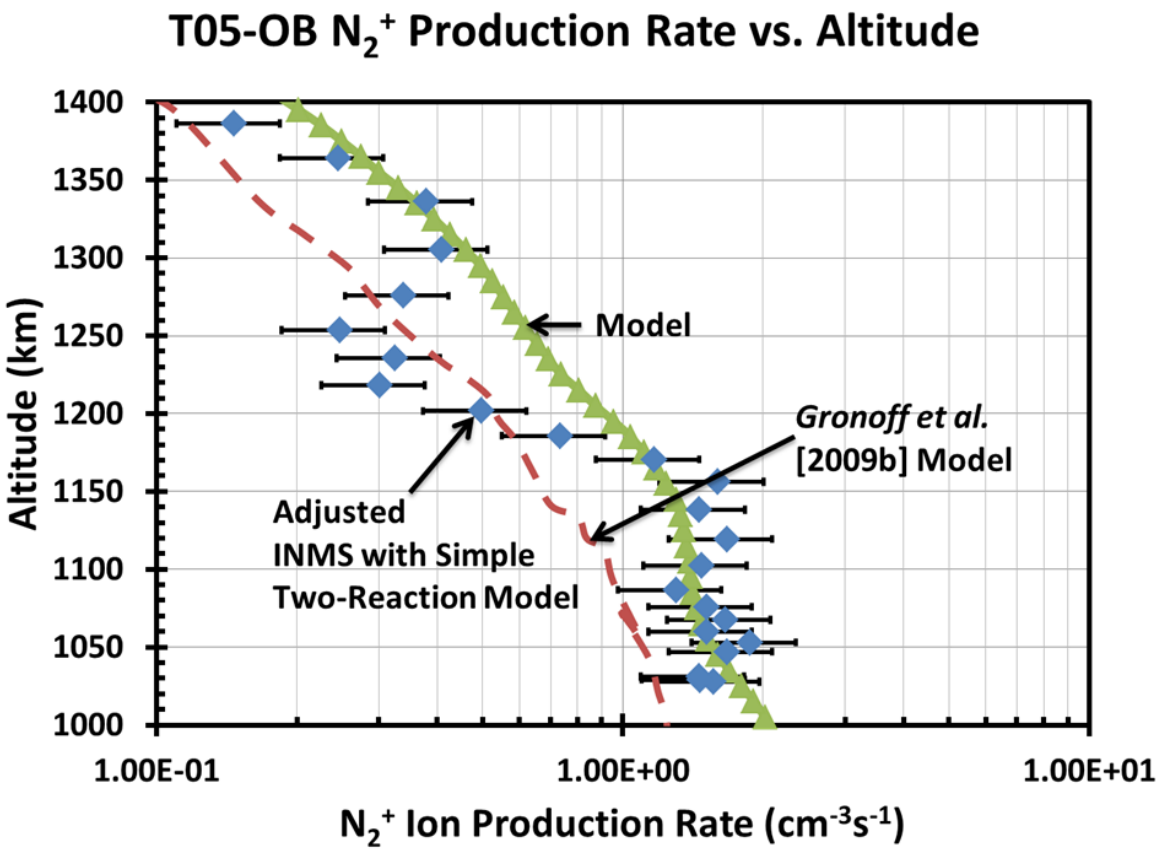

Figure 7: Modeled electron impact production rates of N_2^+ (green triangles) compared to the production rate of N_2^+ derived from INMS data using a simple two – reaction model adjusted by dividing the loss rate of CH_3^+ via reaction with methane by the branching ratio shown in Figure 6 (blue diamonds) for the outbound leg of the T5 flyby of Titan. The modeled production rates of *Gronoff et al*. [2009b] for a radial field line with flux attenuation are also shown (red dashes). A single parabolic field line anchored at the surface of Titan is used for the magnetic field line topology.

874

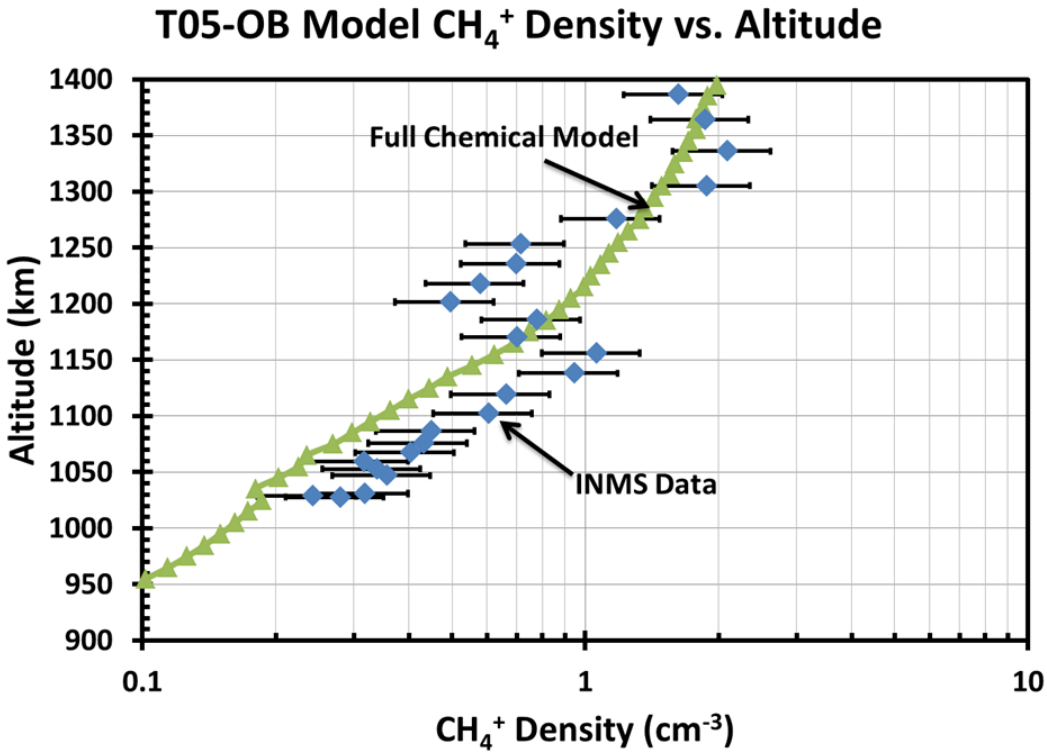

Figure 8: CH_4^+ density produced with the full photochemical model (green triangles) compared to INMS data (blue diamonds) from the T5-Outbound flyby of Titan. A single parabolic field line anchored at the surface of Titan is used for the magnetic field line topology.

875

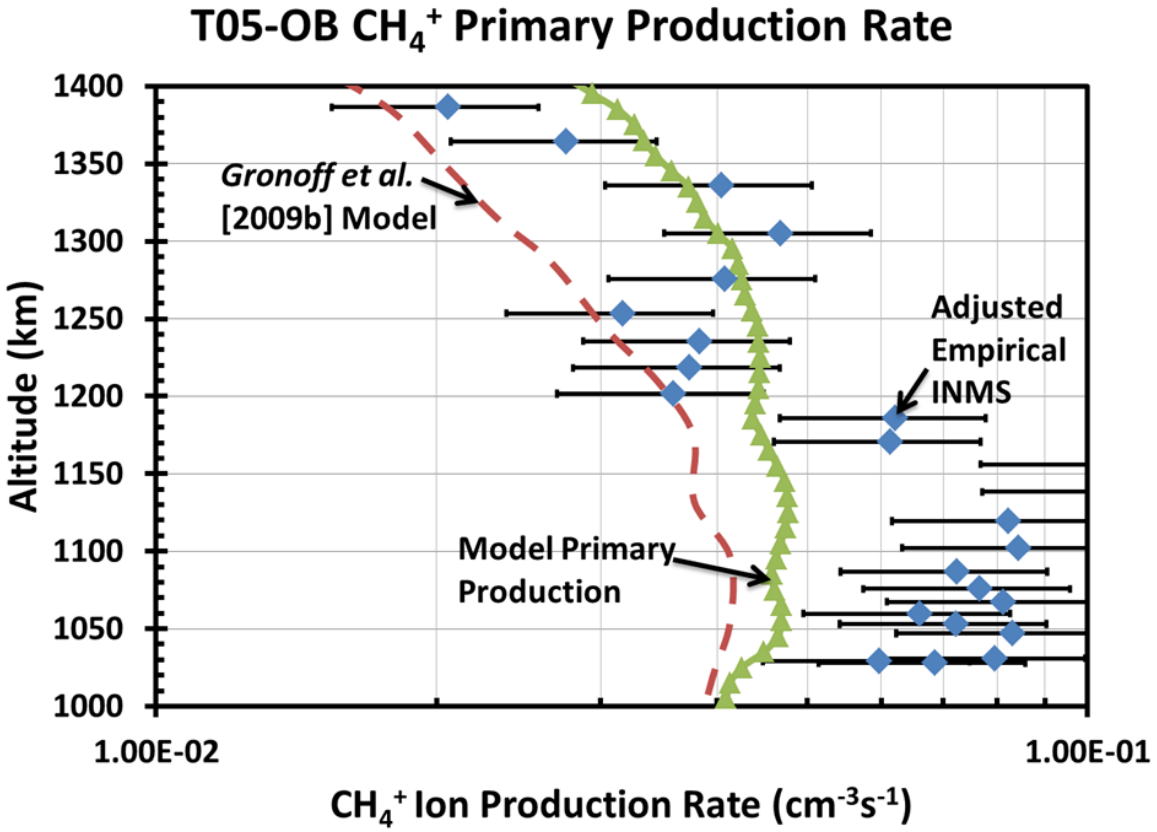

Figure 9: Shown here are modeled production rates (green triangles) of CH_4^+ compared to the empirical production rate of CH_4^+ derived from INMS data (blue diamonds) using the simple two-reaction chemical model for the T5-Outbound flyby of Titan and adjusted by dividing the loss rate of CH_4^+ via reaction with methane by the branching ratio shown in Figure 6. The modeled production rates of *Gronoff et al*. [2009b] for a radial field line with flux attenuation are also shown (red dashes).

876

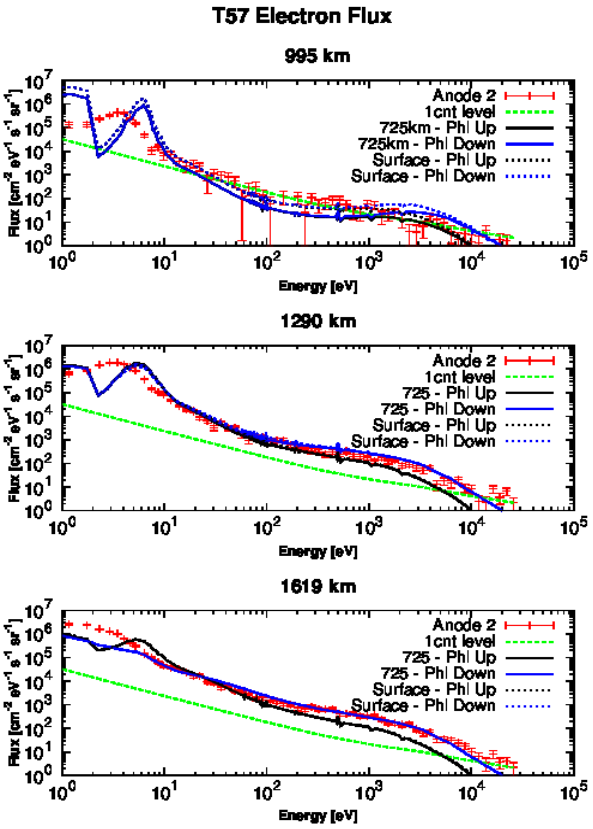

Figure 10: Comparisons between modeled electron fluxes and those measured by CAPS during the T57 encounter at 995 km (top), 1290 km (middle) and 1619 km(bottom). Measurements taken by CAPS-ELS anode 2 are shown in red, modeled fluxes up (black) and down (blue) are shown for parabolic field lines anchored at 725 km (solid) and the surface of Titan (dashed). The CAPS-ELS one count level is shown with a green line.

877

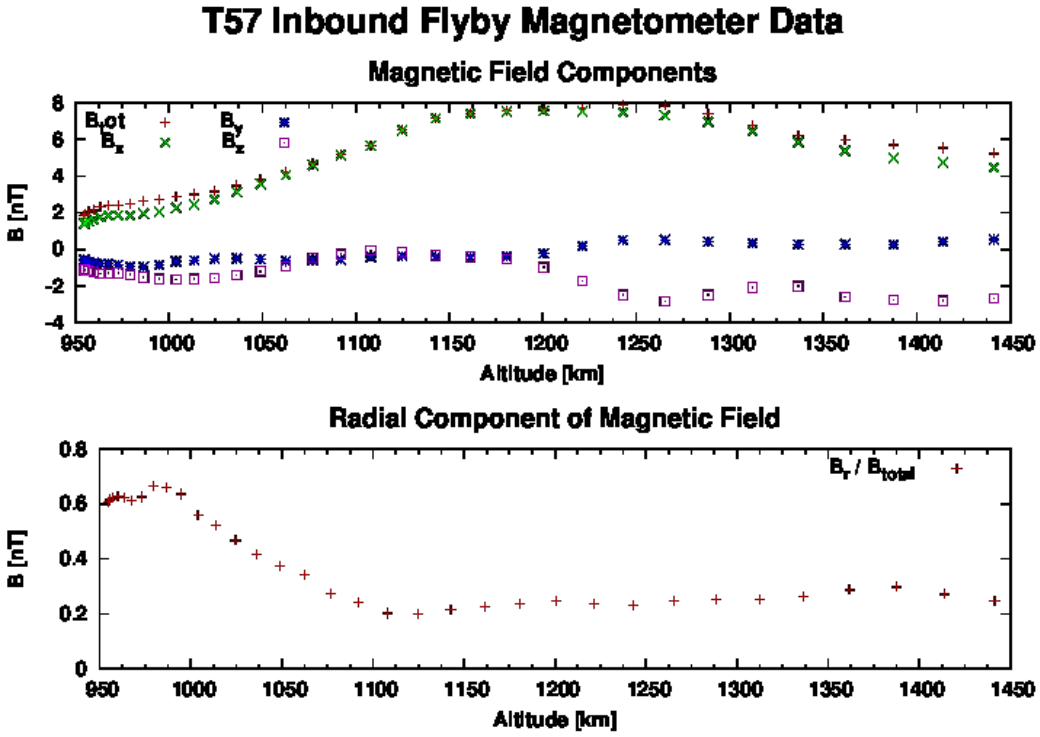

Figure 11: Magnetometer data taken by the MAG instrument aboard Cassini during the T57 flyby. Magnetic field components in TIIS coordinates are shown (top) as well as the ratio of the radial component to the total magnitude of the magnetic field (bottom).

878

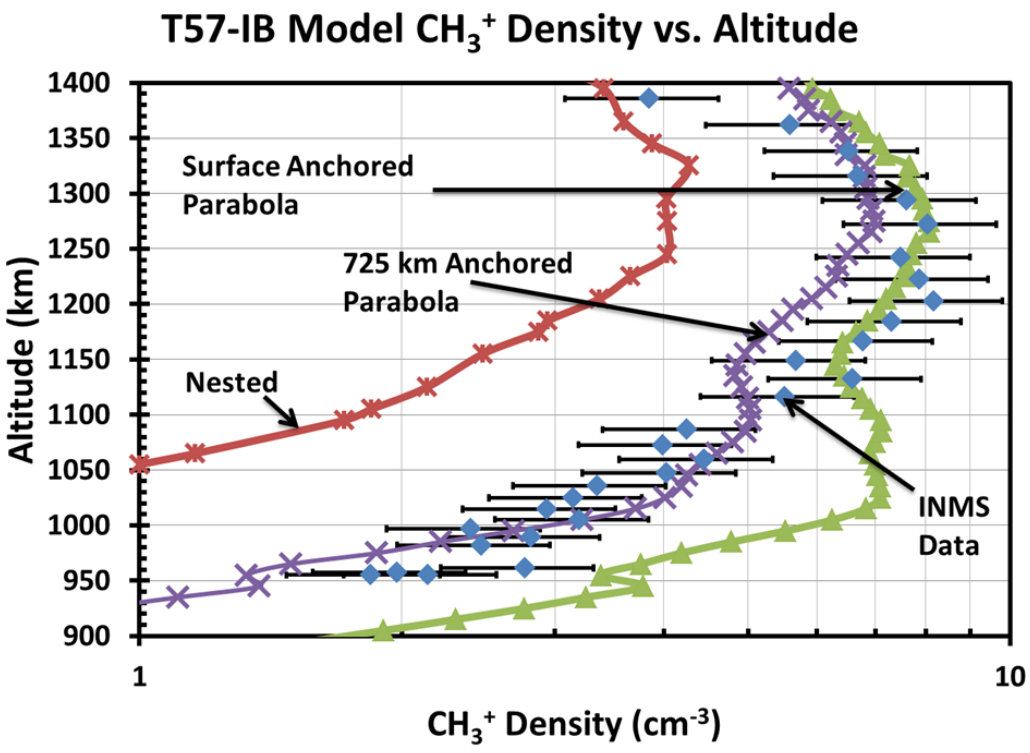

Figure 12: CH_3^+ density produced by the full photochemical model with magnetic field line topologies of a parabola anchored at the surface of Titan (green triangles), a parabola anchored at 725 km (purple crosses) and nested parabola (red stars) using the T57 magnetospheric electron flux measured by CAPS ELS [*Kliore et al.*, 2011] as an input (Figure 10) compared to INMS data from the T57-Outbound flyby of Titan. INMS data is indicated with the blue diamonds. Note that although the surface-anchored parabola is more favored above 1100 km, the 725 km parabola appears to give better agreement below that altitude.

879

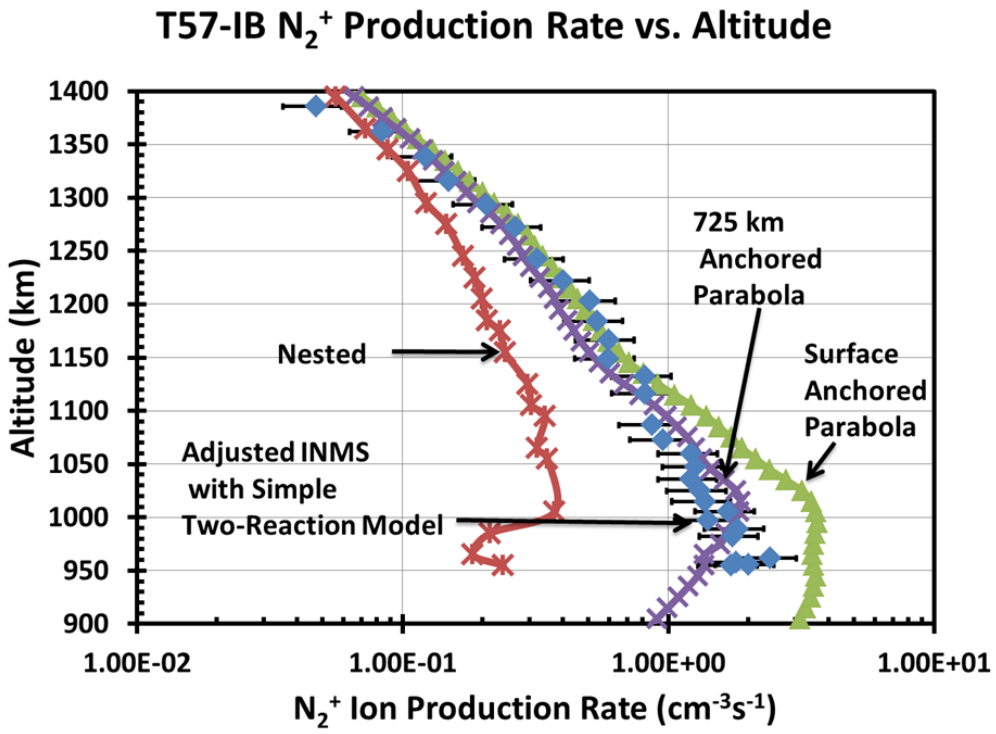

Figure 13: Modeled photoionization production rates of N_2^+ with magnetic field line topologies of a parabola anchored at the surface of Titan (green triangles), a parabola anchored at 725 km (purple crosses) and nested parabola (red stars) compared to the production rate of N_2^+ derived from INMS data using a simple two – reaction model adjusted by dividing the loss rate of CH_3^+ via reaction with methane by the branching factor shown in Figure 6 (blue diamonds) for the inbound leg of the T57 flyby of Titan.

880

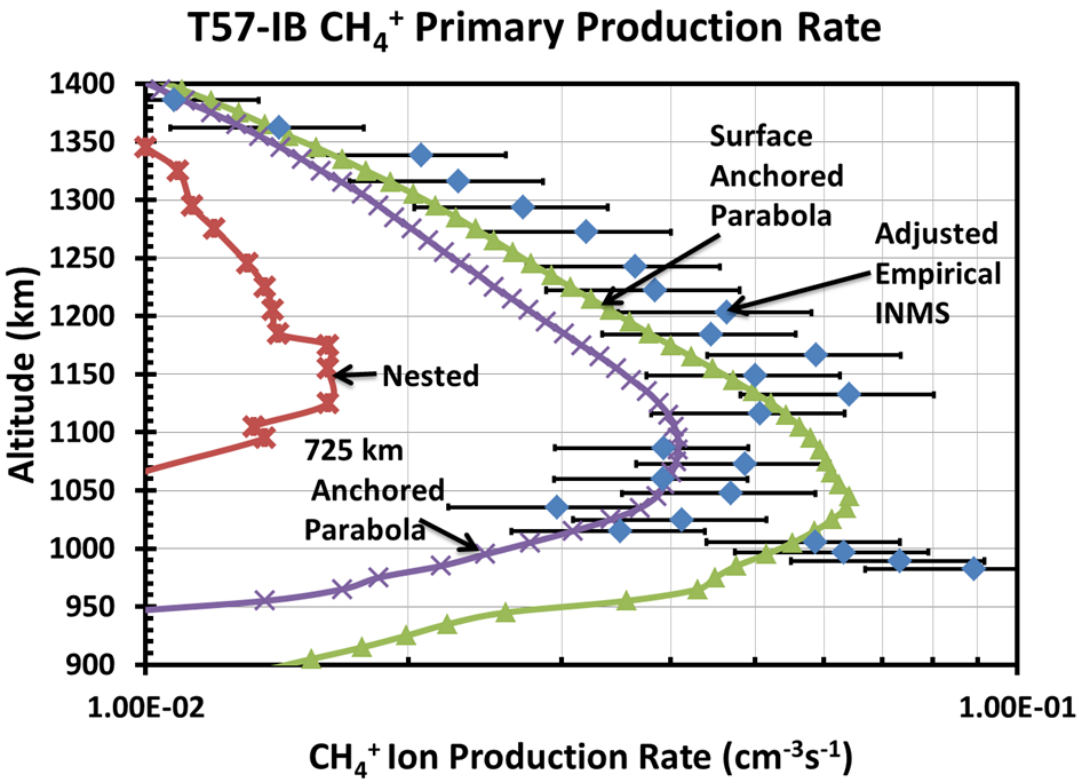

Figure 14: Modeled production rates of CH_4^+ with magnetic field line topologies of a parabola anchored at the surface of Titan (green triangles), a parabola anchored at 725 km (purple crosses) and nested parabola (red stars) using the full photochemical model compared to the empirical production rate of CH_4^+ derived from INMS data (blue diamonds) calculated by dividing the loss rate of CH_4^+ via reactions with methane by the branching ratio shown in Figure 6 for the T57-Inbound flyby of Titan.

881

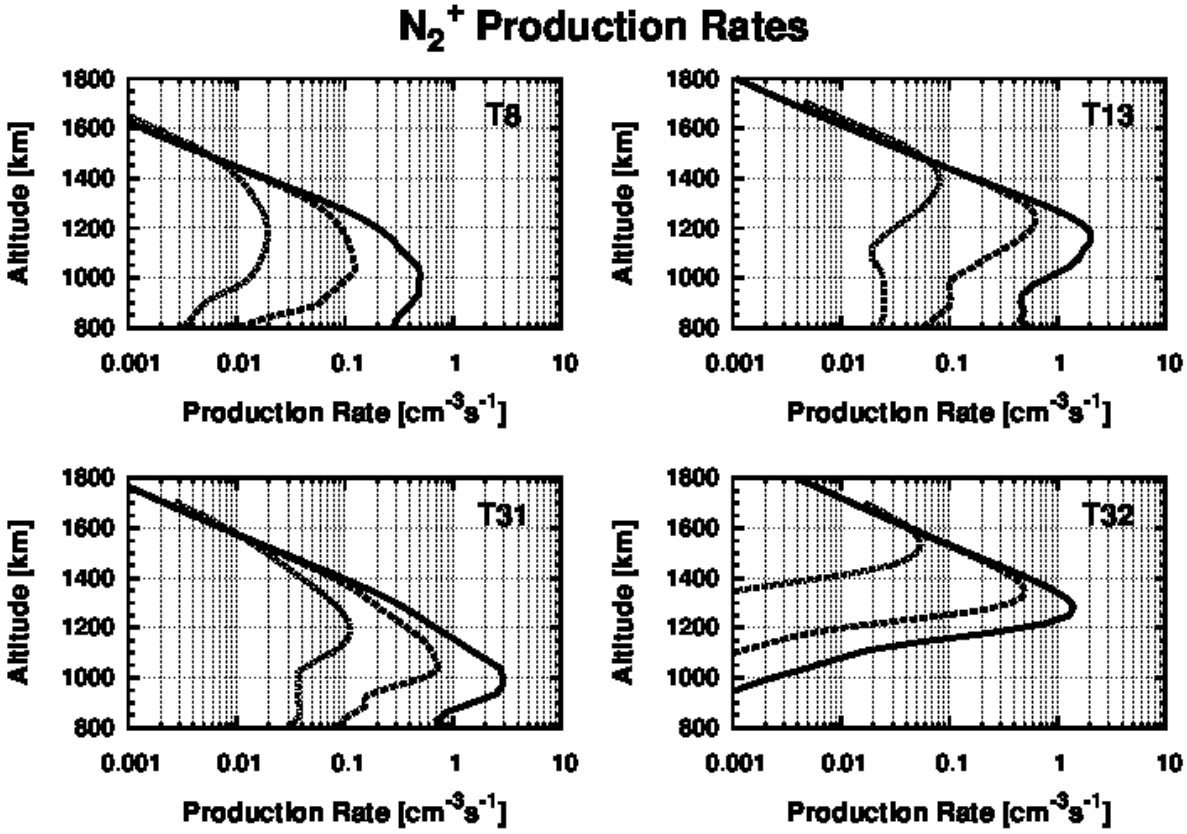

Figure 15: Production of N_2^+ using nested (dotted grey), parabolic (dashed) and radial (solid) magnetic field lines and the magnetospheric electron fluxes of the *Rymer et al.* [2009] classifications. Results are shown for model runs using the T8 lobe-like, T13 plasmasheet, T31 bimodal and the T32 magnetosheath electron fluxes measured by CAPS/ELS. The magnetospheric electron flux profiles are shown in Figure 1.

882

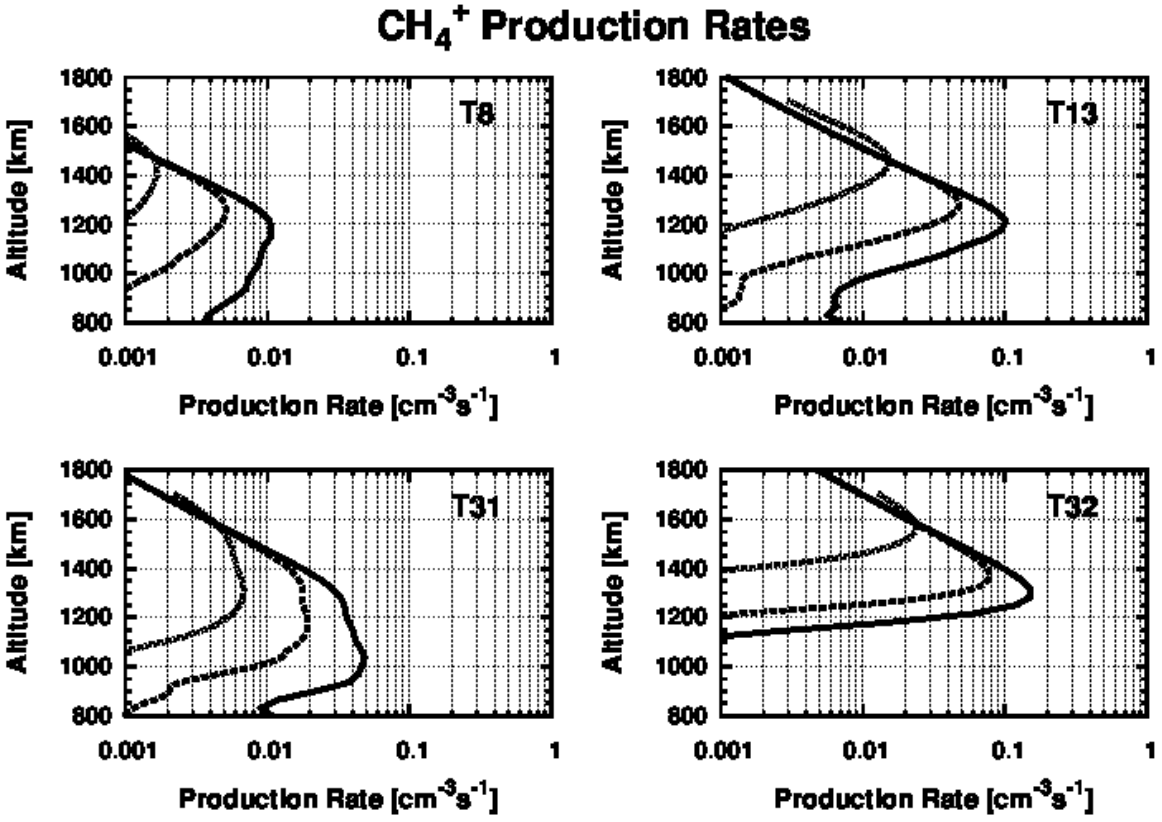

Figure 16: Primary production of CH_4^+ using nested (dotted grey), parabolic (dashed), and radial (black) magnetic field lines and the magnetospheric electron fluxes of the *Rymer et al.* [2009] classifications. Results are shown for model runs using the T8 lobe-like, the T13 plasmasheet, the T31 bimodal, and the T32 magnetosheath electron fluxes measured by CAPS ELS. The magnetospheric electron flux profiles are shown in Figure 1.

883

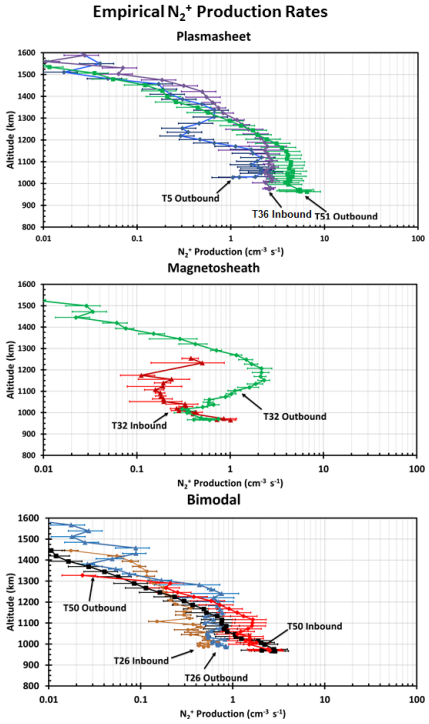

Figure 17: Empirical production rates for N_2^+ derived using the simple two-reaction model (Equation 1), INMS measured densities and an adjustment factor of 0.67. Production rates are generated for nightside flybys classified as plasmasheet (top), magnetosheath (middle) and bimodal (bottom) electron fluxes. Error bars represent uncertainties in INMS measured densities.

884

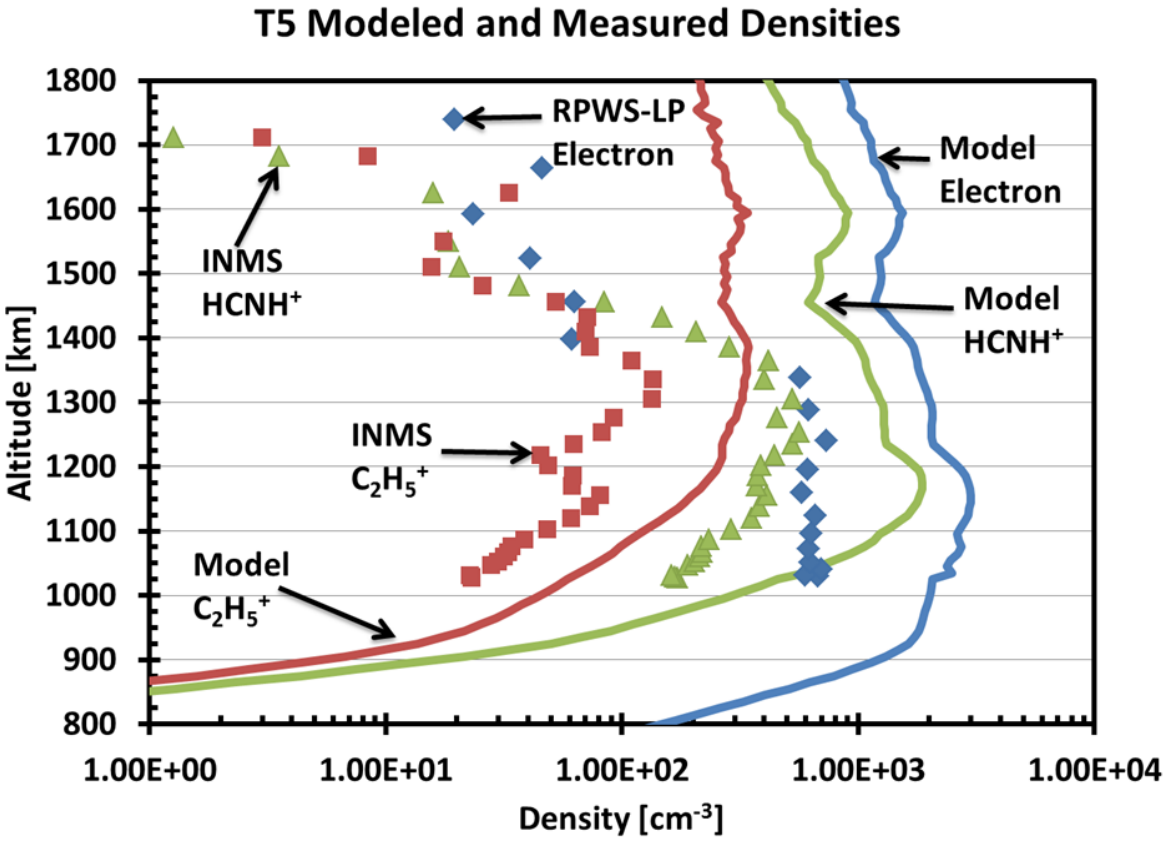

Figure 18: Comparisons between RPWS-LP measured (blue diamonds) and modeled electron densities (blue line) and INMS measured (lines) and modeled densities of $HCNH^+$ (green triangles) and $C_2H_5^+$ (red squares).

885